



Raytheon

SUSPENDED MATTER

VISIBLE/INFRARED IMAGER/RADIOMETER SUITE

ALGORITHM THEORETICAL BASIS DOCUMENT

Version 5: March 2002

Eric Vermote
University of Maryland

Scott Vibert
Heather Kilcoyne
Doug Hoyt
Tom Zhao

RAYTHEON SYSTEMS COMPANY
Information Technology and Scientific Services
4400 Forbes Boulevard
Lanham, MD 20706

SBRS Document #: Y2390

EDRs: SUSPENDED MATTER

Doc No: Y2390

Version: 5

Revision: 0

	FUNCTION	NAME	SIGNATURE	DATE
Prepared By	EDR Developer	E. VERMOTE		1/31/02
Approved By	Relevant Lead	R. SLONAKER		2/8/02
Approved By	Chief Scientist	S. MILLER		2/12/02
Released By	Algorithm Lead	P. KEALY		2/15/02

TABLE OF CONTENTS

LIST OF FIGURES	iii
LIST OF TABLES	v
GLOSSARY OF ACRONYMS	vii
ABSTRACT	ix
1.0 INTRODUCTION	1
1.1 PURPOSE	1
1.2 SCOPE.....	2
1.3 VIIRS DOCUMENTS.....	2
1.4 REVISIONS	2
2.0 EXPERIMENT OVERVIEW	3
2.1 OBJECTIVES OF VIIRS SUSPENDED MATTER RETRIEVALS	3
2.2 BAND CHARACTERISTICS	4
2.3 SUSPENDED MATTER RETRIEVAL STRATEGIES	5
2.3.1 Volcanic Ash	5
2.3.2 Dust/Sand	11
2.3.3 Sea Salt	19
2.3.4 Smoke	19
3.0 ALGORITHM DESCRIPTION.....	23
3.1 PROCESSING OUTLINE	23
3.2 ALGORITHM INPUT	24
3.2.1 VIIRS Data	24
3.2.1.1 Cloud Mask	24
3.2.1.2 Land/Water Mask	24
3.2.1.3 Calibrated TOA Reflectances and Brightness Temperatures	24
3.2.1.4 Aerosol Optical Thickness IP.....	24
3.2.1.5 Angstrom Exponent IP	25
3.2.2 Non-VIIRS Data.....	25
3.2.2.1 Aerosol Index	25
3.3 THEORETICAL DESCRIPTION OF SUSPENDED MATTER RETRIEVALS	25
3.3.1 Quality Check of the Input Data.....	25
3.3.1.1 Physics of the Problem	25
3.3.1.2 Mathematical Description of the Algorithm.....	26
3.3.2 Cloud Check	26

3.3.3	Land/Water Check	26
3.3.4	Volcanic Ash Detection Module.....	26
3.3.5	Dust/Sand Detection Module	27
3.3.6	Sea Salt Detection Module.....	27
3.3.7	Smoke Detection Module.....	27
3.3.8	Second Smoke Detection Module.....	28
3.3.9	Smoke Concentration.....	28
3.3.9.1	Use of Aerosol Optical Thickness Measurements	28
3.3.9.2	Use of VIIRS Smoke Index (SI)	29
3.3.9.3	Conclusions.....	32
3.3.10	Aerosol Types and Aerosol Optical Properties.....	32
3.3.11	EDR Requirements	34
3.3.12	Error Budget.....	35
3.4	ALGORITHM SENSITIVITY STUDIES.....	35
3.4.1	Ash Detection Module	35
3.4.2	Dust/Sand Detection Module	37
3.4.3	Smoke Detection Module.....	40
3.4.4	Comments on Major Errors.....	41
3.5	PRACTICAL CONSIDERATIONS.....	41
3.5.1	Numerical Computation Considerations.....	41
3.5.2	Programming and Procedural Considerations.....	41
3.5.3	Configuration of Retrievals.....	42
3.5.4	Quality Assessment and Diagnostics	42
3.5.5	Exception Handling.....	42
3.6	ALGORITHM VALIDATION.....	42
4.0	ASSUMPTIONS AND LIMITATIONS	45
4.1	ASSUMPTIONS.....	45
4.2	LIMITATIONS.....	45
5.0	REFERENCES	47

LIST OF FIGURES

Figure 1a. An ash cloud (highlighted in green and red) from the eruption of Popocatepl, as distinguished using the 10.8 and 12.0 AVHRR data from 09 December 1998.	7
Figure 1b: RGB of the corrected reflectance observed by MODIS on July, 22, 2001, showing the volcanic ash plume generated by Mt Etna eruption. The red line represents the transect location where reflectance and temperature are plotted on figures 1e and 1f.	8
Figure 1c: Gray level image (0 black, 0.02 white) of the reflectance observed in MODIS band 26 (1.38 μ m), some clouds on the southern part of Italy appears (the highest one) as well as the volcanic ash plume, which indicate it is located relatively high in the atmosphere.	8
Figure 1d: False RGB (R=4.0 μ m, G=1.6 μ m, B=2.13 μ m) showing the very atypical signature of the volcanic ash plume the reflectance at 4.0 μ m is much higher than the one at 1.6 μ m or 2.1 μ m.	9
Figure 1e: Temperatures in MODIS 31 (11 μ m) and 32 (12 μ m) observed on a transect over the volcanic ash plume (see Figure 1b for approximate location of the transect). As expected, the temperature drops over the plume and the difference between 31 and 32 usually positive or close to zero, becomes strongly negative over the plume location.	10
Figure 1f: Result of the simple threshold algorithm (11 μ m –12 μ m <0.1K) to detect volcanic ash plume (mask is the color blue).	11
Figure 2. Nighttime brightness temperatures of VIIRS baseline channels 10 (T10), AERO 1 (TAERO), 11 (T11), and 12 (T12) versus turbidity.	13
Figure 3. Spectral distribution of reflectance (%) over sand. The data is taken from the database of MOSART and interpolated to VIIRS bands.	14
Figure 4. TOA radiance (TOAR) versus turbidity for VIIRS thermal bands for the case shown in Figure 2. The units of the radiance is (Wcm ⁻² ster ⁻¹).	15
Figure 5. The contribution from surface emission (CFSE) versus the TOA radiance for VIIRS thermal bands for the case shown in Figure 2.	16
Figure 6a. The contribution from atmospheric thermal emission (CFATE) versus the TOA radiance for VIIRS thermal bands for the case shown in Figure 2.	16
Figure 6b. The contribution from surface reflected atmospheric thermal emission (CFSRATE) versus the TOA radiance for VIIRS thermal bands for the case shown in Figure 2.	17
Figure 7a: RGB image (no aerosol correction) showing a dust storm (yellow-white) over the Mediterranean sea.	18
Figure 7b: False RGB image (2.1 μ m Blue, 1.6 μ m Green, 3.75 μ m Red), the low clouds appear whiter than the dust in this false RGB.	18
Figure 7c: Experimental dust storm mask. The area detected as strong dust concentration is colored in red-orange.	19
Figure 8. Top - Smoke over Indonesia for 10 April 1998 as seen by SeaWiFS. RGB composite, R=0.67 μ m, G=0.87 μ m, B=Smoke Index. Smoke is blue to violet as	

it is enhanced in the Blue and Red components. Bottom – TOMS Aerosol Index for the same day verifies the SeaWiFS detection of smoke.....	20
Figure 9. Suspended Matter Data Flow Diagram.	23
Figure 10. Smoke concentration ($\mu\text{g}/\text{m}^3$) vs aerosol optical thickness at 550 nm.	29
Figure 11. The Smoke Index simulated using the 6S radiative transfer code versus the aerosol optical depth at 550 nm.	30
Figure 12. Smoke concentration versus the Smoke Index. Note that two possible smoke concentrations exist for each value of the Smoke Index.....	31
Figure 13. Derived ash indices ($\text{BT}_{10.8}-\text{BT}_{12.0}$) for the Ocean case.	38
Figure 14. Derived ash indices for the Land case.	38
Figure 15. Derived ash indices for the Desert case.	39
Figure 16. Derived ash indices for the Snow case.	39
Figure 17. Global smoke index product using smoke detection module on SeaWiFS data for 22 September 1997. The smoke from fires over Indonesia was successfully detected (blue).	41

LIST OF TABLES

Table 1. Summary of suspended matter product.....	1
Table 2. VIIRS Band Characteristics	4
Table 3. VIIRS data required by the suspended matter algorithm	24
Table 4. Non-VIIRS data required by the suspended matter algorithm	25
Table 5. Proposed aerosol type classification scheme for aerosols using the Angstrom coefficients and Smoke Index (SI) as inputs.....	33
Table 6. Aerosol types as a function of Angstrom exponent.	34
Table 7. Suspended Matter System Specification Requirements.....	35
Table 8. MODTRAN Volcanic Models for Different Vertical Distributions and Extinction Models.....	36

GLOSSARY OF ACRONYMS

AERONET	Aerosol Robotic Network
ATBD	Algorithm Theoretical Basis Document
AVHRR	Advanced Very High Resolution Radiometer
CCN	Cloud Condensation Nuclei
CMIS	Conical Scanning Microwave Imager/Sounder
DLI	Dust Loading Index
EDR	Environmental Data Record
FOV	Field of View
GOES	Geostationary Operational Environmental Satellite
IPO	Integrated Program Office
IR	Infrared
LIDAR	Light Detection and Ranging
MODIS	Moderate Resolution Imaging Spectroradiometer
MODTRAN	Moderate Resolution Model for Atmospheric Transmittance/Radiance
NIR	Near Infrared
NPOESS	National Polar-orbiting Operational Environmental Satellite System
OMPS	Ozone Mapping Profiling Suite
QA	Quality Assurance
SDM	Smoke Detection Module
SeaWiFS	Sea-viewing, Wide-field-of-view Sensor
SRD	Sensor Requirements Document
TBD	To Be Determined
TBR	To Be Reviewed
UV	Ultraviolet
VIIRS	Visible/Infrared Imager/Radiometer Suite
WMO	World Meteorological Organization

ABSTRACT

Suspended matter is defined as dust, sand, volcanic ash, sea salt, smoke, and radioactive smoke in the atmosphere. These materials have an important impact on climate change, aviation and military operations, and human health. The VIIRS Suspended Matter EDR provides information that will improve detection of population hazards and reduce the risk to military operations and human life. This information is not currently available on an operational basis. Additionally, this product will provide information for climate change research. The algorithm presented in this document primarily uses the unique spectral signatures of each aerosol type. For example, volcanic ash displays a characteristic increase in radiometric emissivity from 11 μm to 12 μm due to the sulfuric acid present within the ash cloud, smoke is more transparent than clouds in the Near Infrared, and silicate material in dust/sand displays obvious absorption near 8.35 μm . The retrieval algorithm combines the unique spectral properties of each type of suspended matter with aerosol optical thickness, particle size parameter, and geolocation to classify the suspended matter globally. Because of the availability of the aerosol model information in the aerosol EDRs, smoke, sea salt, dust type can be directly mapped from the smoke, dust and oceanic aerosol model (see Aerosol EDRs Algorithm Theoretical Basis Document Y2388). For other type of suspended matter or when the aerosol model inversion fails, aerosol particle size information and visible and infrared techniques are used for detection. The retrieval program is modularized, with a module for each suspended matter type. The smoke, dust, and volcanic ash detection modules are discussed in detail. There is no direct pathway for identification of radioactive smoke and therefore it will not be discussed in this version of the ATBD.

1.0 INTRODUCTION

Suspended matter plays an important role in climate change and can have a major impact on human health and military operations. Aerosols affect the Earth's radiative balance (Charlson *et al.*, 1992; Bolin *et al.*, 1994) directly and indirectly. Aerosol forcing is opposite in magnitude to the forcing of greenhouse gases. The uncertainty in aerosol forcing is considered to be one of the largest uncertainties in modeling climate change because of the shortage of global aerosol distribution information. This is true especially for those aerosols with large spatial and time variability, such as smoke, sand storms, dust, and nuclear debris. Detection of these highly variable aerosols is challenging because of their short lifetime, small scale, and strong interactions with surface albedo and local meteorological conditions.

Both visible and infrared (IR)-based techniques have been applied for detection of suspended particles in the atmosphere (Kaufman *et al.*, 1997; Tanre and Legrand, 1991; Ackerman, 1997). Visible techniques derive aerosol loading from path radiance, which is obtained by subtracting the surface contribution from the apparent reflectance measured by the sensor. IR detection techniques are based on the facts that aerosols display strong spectral variations in IR regions and that the atmosphere is fairly transparent in these spectral regions. If aerosol loading is thin, transmitted surface emissions become the major component of the detected signal. If aerosol loading is thick, aerosol emissions account for a major part of the measurement. In practice, the analysis is based on brightness temperature rather than radiance. The magnitude of the difference in brightness temperatures in selected IR channels can be used to infer the signature of aerosol loading. Our detection algorithms for suspended matter combine aerosol model information, aerosol optical thickness and particle size parameter information with visible and IR techniques, which will be described in detail in this document.

1.1 PURPOSE

This Algorithm Theoretical Basis Document (ATBD) describes the algorithm used to retrieve the Suspended Matter Environmental Data Record (EDR) for the Visible/Infrared Imager/Radiometer Suite (VIIRS) on the National Polar-orbiting Operational Environmental Satellite System (NPOESS). This product is summarized in Table 1. Specifically, this document identifies sources of input data, both VIIRS and non-VIIRS that are required for retrieval; provides the physical theory and mathematical background underlying the use of this information in the retrievals; provides implementation details; and describes assumptions and limitations of the proposed approach.

Table 1. Summary of suspended matter product.

Parameter Name	Horizontal Cell Size	Comments
Suspended Matter	1.6 km	<ul style="list-style-type: none">• Will flag cells containing suspended matter in the atmosphere• Will type aerosol within horizontal cell• Will be retrieved globally• Will derive smoke concentration

1.2 SCOPE

This document covers the algorithm theoretical basis for retrieval of the suspended matter product of VIIRS on NPOESS. Modifications to the approach may occur as validation is performed during Phase 2.

Section 1 describes the purpose and scope of the document. Section 2 provides a brief overview of the suspended matter retrieval. The theoretical description and implementation of the algorithm are described in Section 3, and the assumptions and limitations of the approach are summarized in Section 4. References for citations in the text are listed in Section 5.

1.3 VIIRS DOCUMENTS

Reference to VIIRS Project or reference documents is indicated by a number in italicized brackets as follows, e.g., *[V-1]*.

[V-1] Visible/Infrared Imager/Radiometer Suite (VIIRS) Sensor Requirements Document (SRD) for National Polar-orbiting Operational Environmental Satellite System (NPOESS) Spacecraft and Sensors.

[V-2] VIIRS Aerosol Optical Thickness and Size Parameter Algorithm Theoretical Basis Document, Doc. # Y2388.

[V-3] VIIRS System Validation and Verification Plan, Doc. #Y3270.

[Y3257] VIIRS Computer Resources Requirements Document

1.4 REVISIONS

This is the fifth version of this document and is dated March 2002. The change from the previous version is that an aerosol model (from Aerosols EDRs) is the preferred path to identify dust, smoke and sea salt cases, the volcanic ash and heavy dust detection techniques have been tested against VIIRS like data (MODIS). In previous revisions, elaboration on the detection methods for volcanic ash and dust were added and simulation study results for ash and dust were also added as well as computation of smoke concentration. The first version of this document was dated October 1998.

2.0 EXPERIMENT OVERVIEW

2.1 OBJECTIVES OF VIIRS SUSPENDED MATTER RETRIEVALS

Suspended matter is defined as dust, sand, volcanic ash, sea salt, and smoke located in the atmosphere. These materials have an important impact on climate change, flight operations, and human health. The VIIRS Suspended Matter EDR will use the VIIRS Aerosol Optical Thickness and Particle Size Parameter EDRs in combination with the properties of the types to classify aerosols globally at a horizontal resolution of 1.6 km.

The purpose of the suspended matter algorithm is to classify observed particle events and estimate the mass loading at a reasonable resolution. This will be accomplished by looking for the spectral signatures unique to the types in conjunction with the aerosol optical depth and size parameter at that location. The importance of classifying the suspended matter varies by type. For example, the detection of volcanic ash is very important for several reasons. Two of the most powerful eruptions of the century have occurred within the past 20 years: El Chichón in 1982 and Mt. Pinatubo in 1991 (Bredow *et al.*, 1995). Eruptions of volcanoes eject aerosols and fine ash into the atmosphere where they stay for extended time periods. In the atmosphere, they act as additional scatterers and absorbers, thus affecting the Earth's radiation budget. It has been estimated that the Mt. Pinatubo eruption in June 1991 reduced the average net radiation at the top of the atmosphere by 2.5 W/m^2 for 2 to 4 years, yielding 0.5°C cooling regionally, and $0.2\text{-}0.3^\circ\text{C}$ cooling globally (Simarski, 1992; Stowe *et al.*, 1992; Ardanuy *et al.* 1986). In addition to increasing the concentration of scattering and absorbing particles in the atmosphere, the volcanic gases emitted may react with anthropogenic CFC's to accelerate the destruction of stratospheric ozone. One data set credits the Mt. Pinatubo eruption with a 15-20 percent loss of ozone at high latitudes (Bredow *et al.*, 1995). One of the most important reasons for a satellite ash detection product is the hazard posed to aviation. Jet engines have failed after flying through ash clouds, as the hot ash damages the engine by eroding moving parts and accumulating on surfaces of the engine (Bredow *et al.*, 1995).

Another reason for classifying suspended matter is the diverse effects suspended matter may have on clouds in the area. The different kinds of suspended matter can interact with the background cloud condensation nuclei (CCN) according to their size, and increase or decrease the amount and size of clouds in the area, thus altering the amount of solar radiation received.

The overall objectives of the VIIRS suspended matter retrieval are:

- 1) To flag cells containing suspended matter in the atmosphere.
- 2) To determine the type of suspended particles in an area from their optical thickness, size parameter, radiance and reflectance measurements, brightness temperature, and other available information.
- 3) To obtain smoke concentration when smoke is present.

2.2 BAND CHARACTERISTICS

The narrow band measurements of the VIIRS sensor in the 0.4 to 3.70 μm range are used to derive aerosol optical thickness. The aerosol algorithm uses a dynamic aerosol model for aerosol inversion selecting the model that better fits the signal observed at specific wavelengths (412nm, 445nm, 488nm, 672nm over land; 865nm, 1240nm, 1610nm, 2250nm over Ocean). The inversion maps directly to the smoke, dust and sea salt suspended matter categories. In case the inversion fails, the angstrom exponent, optical thickness and spectral indices are used for identification of suspended matter. In the case of volcanic ash, since no specific aerosol model has been defined so far, only spectral methods can be used for inversion. The visible and near-IR channels used to derive optical thickness are all within window regions, and their bandwidths are narrow, so that the contamination of gas (such as O_2 , O_3 , H_2O) absorption is minimized in direct measurements. The suspended matter algorithm uses techniques involving not only visible and near-IR channels, but also four IR channels (3.70, 8.55, 10.8, and 12 μm). Aerosols display strong spectral variations in these thermal spectral regions, and the atmosphere is also fairly transparent here. Thus, the signature of the aerosol emissions will be detectable by the sensor, especially when the aerosol loading is thick.

Table 2. VIIRS Band Characteristics

Band Name	Wavelength (μm)	Bandwidth (μm)
M1	0.412	0.0200
M2	0.445	0.0180
M3	0.488	0.0200
M4	0.555	0.0200
M5	0.672	0.0200
M6	0.746	0.0150
M7	0.865	0.0390
M8	1.240	0.0200
M9	1.378	0.0150
M10	1.610	0.0600
M11	2.250	0.0500
M12	3.700	0.1800
M13	4.050	0.1550
M14	8.550	0.3000
M15	10.7625	1.0000
M16	12.0125	0.9500

2.3 SUSPENDED MATTER RETRIEVAL STRATEGIES

In lieu of the classification obtained by the model inversion, we can classify aerosols by looking at the spectral dependence of the optical depths on observed aerosol reflectances. Each type of suspended matter has a unique spectral signature, resulting from either particle size or chemical composition. The algorithm will test each pixel in parallel for the presence of dust/sand, ash, smoke, or sea salt. If this information is not enough for an accurate classification, information on geolocation may be used. This would aid in the routine identification of sea salt or sand, or special event identification of volcanic ash. The various tests for the types of suspended matter use the majority of the VIIRS bands, including bands at 0.412, 0.445, 0.488, 0.555, and 0.672 μm for smoke detection; 1.378 μm for detection of stratospheric aerosols; 4.05, 10.8, and 12.0 μm for detection of volcanic ash; and 3.7, 10.8, 12.0, and 8.55 μm for dust detection and for the separation of dust from sand. The objective requirements for this EDR listed in the SRD [V-1] specify the classification of aerosols within layers of the atmosphere. It is impossible using VIIRS channels alone, but the UV bands from the Ozone Mapping Profiling Suite (OMPS) may be used synergistically for additional information on absorption of the aerosols and the vertical profile once technical details of the sensor and EDR specifications are released.

Each suspended matter type requires a specific test. The modules included in the current version of the algorithm are a smoke detection algorithm, a dust detection algorithm, and a volcanic ash detection algorithm. The smoke detection algorithm is based on the scheme developed by Eric Vermote for Sea-viewing Wide-field-of-view Sensor (SeaWiFS) data (Vermote *et al.*, 2001); it uses the differences in the sensitivities of the visible channels to construct a smoke index indicating the location of smoke. Smoke concentration is also derivable from the smoke index. The dust and ash detection algorithms are based on spectral contrast techniques. These algorithms will be explained in greater detail later in this document. Later versions of the algorithm will include modules to test for the presence of the other types of suspended matter within a horizontal cell.

2.3.1 Volcanic Ash

Volcanic ash is considered to be any type of suspended matter containing sulfuric acid (H_2SO_4). Sulfuric acid forms and coats the small ash particles within a volcanic ash cloud. This occurs when the ice/water droplets within the cloud combine with the smaller ash particles, as the cloud disperses over time, when the larger ash particles fall out of the cloud due to gravity. Volcanic ash clouds have been demonstrated to have not only strong effects on the climate system (e.g., Pollack *et al.*, 1976), but also the potential hazard for private, military, and commercial aircraft. There have been more than 80 reports of aircraft entering ash clouds in the past 20 years (<http://www.geo.mtu.edu/departments/classes/ge404/gcmayber/intro.html>). Major air routes are threatened by hundreds of potentially active volcanoes, many of them in the north and west Pacific and many of which are not monitored. Although ash clouds have not caused any aviation deaths yet, the number of potentially active volcanoes within major air routes leads many researchers to believe that the lack of operational volcanic cloud detection is a disaster waiting to happen.

A nascent volcanic eruption cloud consists of large ash particles (0.1-100 μm) with short residence times and highly variable vertical distribution. Dispersed volcanic clouds consist

largely of smaller sulfuric acid coated particles ($\leq 0.1\mu\text{m}$) with long residence time and relatively uniform vertical distribution. The techniques used to detect particles in these two phases may be different because of different characteristics of the particles in the two regimes.

The radar systems on the ground and onboard aircraft are widely used for monitoring ash clouds, especially for nascent volcanic eruption clouds. The ground-based radar systems are only useful during the eruption and up to about 30 minutes after the eruption (Harris and Rose, 1983; Rose *et al.*, 1995a). They are normally located near cities, away from most volcanoes. The radar systems onboard aircraft are similar to those of ground-based systems. More information regarding the vertical distribution of the clouds can be obtained by comparing aircraft measurements with ground-based systems. However, similar to ground-based systems, they are still unable to detect volcanic ash clouds several hours after the eruption due to the small size of dispersed volcanic ash particles. Poor visibility or darkness may impede visual detection by the flight crew as well.

The absorbance properties of volcanic ash in the 10-12 μm window have led to an ash detection technique using two channels in this window. This technique, currently being used with Geostationary Operational Environmental Satellite (GOES) and Advanced Very High Resolution Radiometer (AVHRR) data, uses a brightness temperature difference between the two channels to differentiate between a meteorological cloud (ice or water cloud) and an ash cloud. The volcanic clouds typically have a negative brightness temperature difference when AVHRR band 5 (11.5 to 12.5 μm) is subtracted from band 4 (10.3 to 11.3 μm) while meteorological clouds generally have a positive brightness temperature difference. (Prata, 1989) The magnitude of the negative difference of the volcanic clouds is dependent on the optical thickness and composition of the cloud. This band subtraction technique was developed by Prata (1989) and Wen and Rose (1993) and has been shown to work with GOES and AVHRR data. This technique will be used on VIIRS with bands M15 (10.2625 to 11.2625 μm) and M16 (11.5375 to 12.4875 μm).

The theory for the “split window” volcanic ash cloud detection technique arises from observations of ash clouds by Prata (1989). A distinction is made between the initial eruption cloud, which is optically thick, high, and a mixture of ash and ice/water droplets which makes the spectral signal similar to that of meteorological clouds, and the dispersed cloud (older than about 12 hours). The dispersed cloud is thinned by gravity as the larger ash particles fall out and H_2SO_4 has formed and coated the smaller ash particles left within the cloud. It is known that the extinction for H_2SO_4 aerosol is less at 12 μm than at 11 μm , which is opposite that of water. This opposite effect allows discrimination between dispersed volcanic clouds and water/ice clouds. The eruption cloud, the cloud before it is dispersed, may also exhibit the negative brightness temperature difference due to the presence of H_2SO_4 droplets. Because the cloud still contains an abundance of ice/water droplets and the H_2SO_4 may not be evenly distributed throughout the cloud, the method is not as effective on fresh clouds.

Simulations have been performed using the Moderate Resolution Model for Atmospheric Transmittance/Radiance (MODTRAN). The 8 levels of ash extinction were compared to the brightness temperature produced assuming no ash presence and cirrus and cumulus clouds. The results are presented in the sensitivity studies section. Real data must be analyzed to further test this method. AVHRR has been used with much success to track volcanic ash clouds and is now being used operationally for aircraft safety. An example of our ash detection technique using AVHRR data from the Popocateptl volcano in Mexico is shown in Figure 1a.

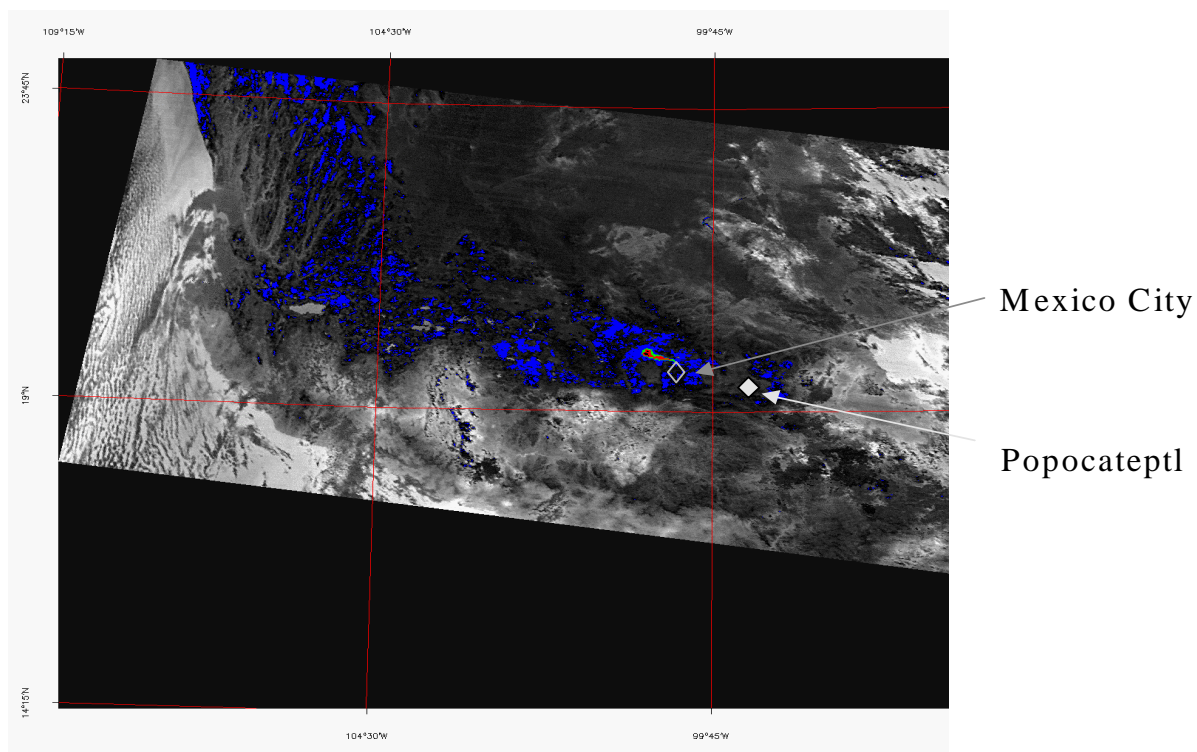


Figure 1a. An ash cloud (highlighted in green and red) from the eruption of Popocatepetl, as distinguished using the 10.8 and 12.0 AVHRR data from 09 December 1998.

MODIS has also been able to observe the Etna eruption and the volcanic ash plume produced. The data presented hereafter were acquired on July 22, 2001 at 9:55GMT. Figure 1b shows RGB images of the corrected reflectance over the Mt Etna area. One can clearly see the volcanic ash plume originating from the volcano, which is of a grey redish color. That plume is located relatively high in the atmosphere as it is detected by the band 26 ($1.38\mu\text{m}$), see Figure 1c. On Figure 1d, we show a false RGB ($R=4.0\mu\text{m}$, $G=1.6\mu\text{m}$, $B=2.25\mu\text{m}$) of the same location using the short wave and middle infrared reflectance ($4.0\mu\text{m}$) bands. In this wavelength combination, the volcanic ash plume appears bright red.



Figure 1b: RGB of the corrected reflectance observed by MODIS on July, 22, 2001, showing the volcanic ash plume generated by Mt Etna eruption. The red line represents the transect location where reflectance and temperature are plotted on figures 1e and 1f.

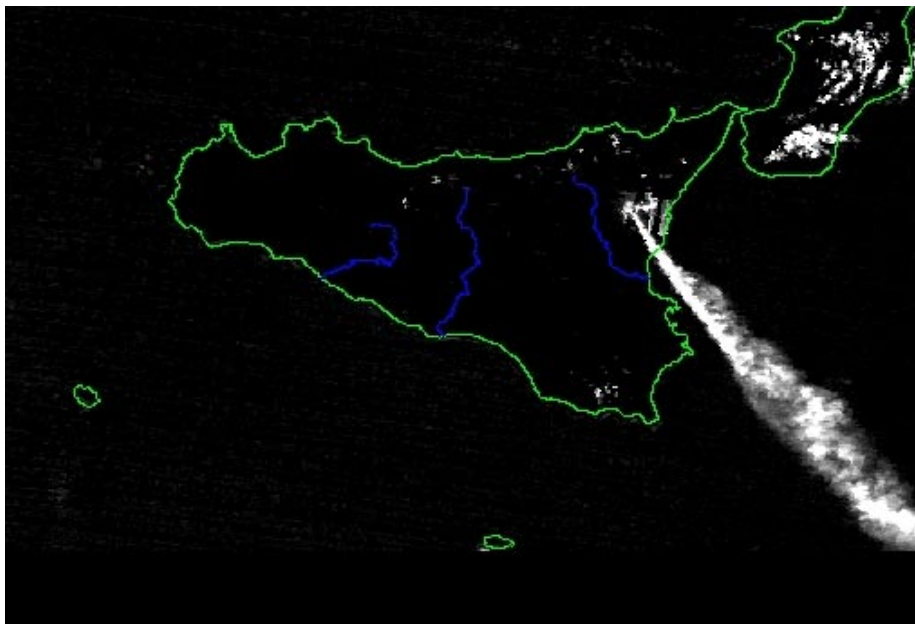


Figure 1c: Gray level image (0 black, 0.02 white) of the reflectance observed in MODIS band 26 ($1.38\mu\text{m}$), some clouds on the southern part of Italy appears (the highest one) as well as the volcanic ash plume, which indicate it is located relatively high in the atmosphere.



Figure 1d: False RGB (R=4.0 μ m, G=1.6 μ m, B=2.13 μ m) showing the very atypical signature of the volcanic ash plume the reflectance at 4.0 μ m is much higher than the one at 1.6 μ m or 2.1 μ m.

Finally, we present in Figure 1e over a transect crossing the volcanic ash plume, the value of the temperature observed in band 31 (11 μ m) and 32 (12 μ m). As observed by Prata (1989), the temperature over the volcanic ash plume decreases as it does over cloud, but unlike for water clouds, the difference between 31 and 32 becomes strongly negative (here 1-2K). Figure 1f shows the detection of volcanic using a single threshold (-0.1K) on the difference between 11 μ m and 12 μ m to detect volcanic ash. Figure 1f shows that this simple approach performs well on that example, the clouds on the southern part of Italy are not detected as volcanic ash, the red area over land at the source of the plume correspond to lava flow showing as well an enhanced response at 4.0 μ m (see fire detection in aerosol ATBD) but no signal at 1.38 μ m and a higher temperature than the volcanic ash plume (around 300K vs. 280K for the plume).

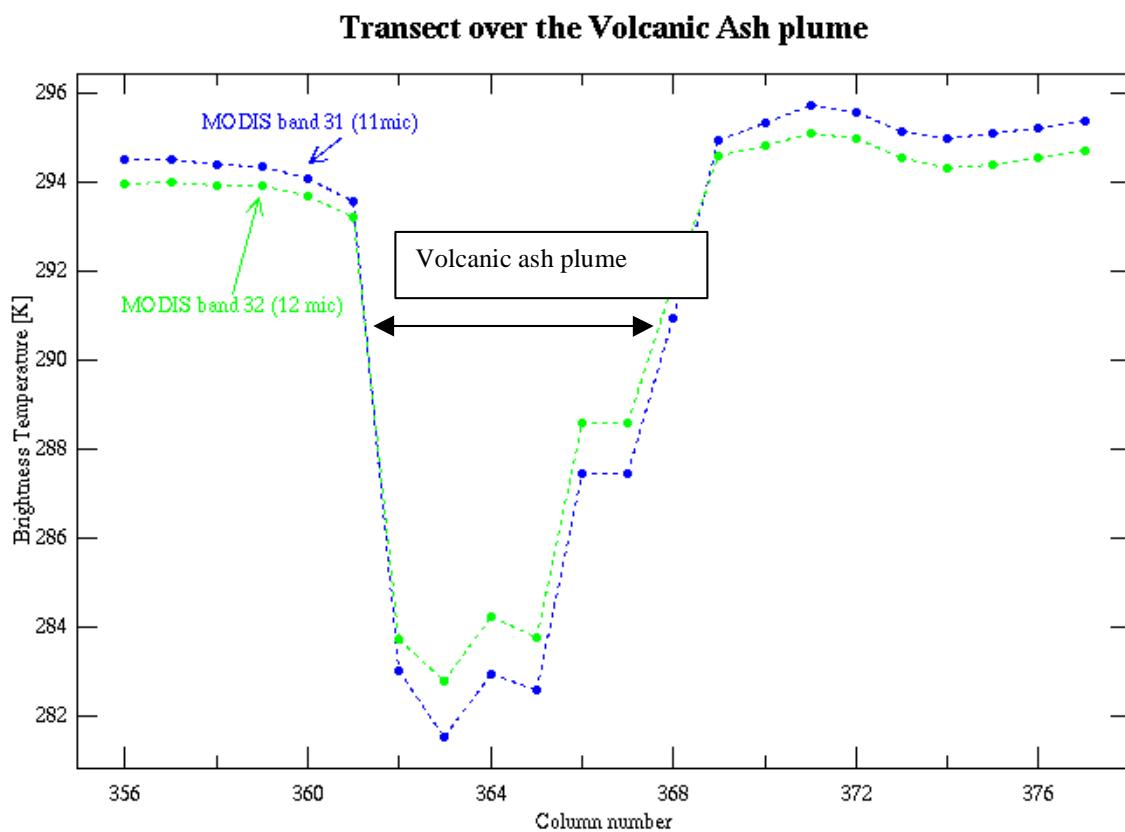


Figure 1e: Temperatures in MODIS 31 (11 μ m) and 32 (12 μ m) observed on a transect over the volcanic ash plume (see Figure 1b for approximate location of the transect). As expected, the temperature drops over the plume and the difference between 31 and 32 usually positive or close to zero, becomes strongly negative over the plume location.



Figure 1f: Result of the simple threshold algorithm ($11\mu\text{m} - 12\mu\text{m} < 0.1K$) to detect volcanic ash plume (mask is the color blue).

2.3.2 Dust/Sand

Dust/sand particles have an Angstrom exponent less than 0.5 and are likely to be the dominant aerosol type for optical thickness greater than 0.25. If the Angstrom exponent is between 0.0 and 0.5, and the optical thickness is between 0.15 and 0.25, the aerosol is likely to be a mixture of maritime and desert aerosols. The effects of dust on climate forcing has caught the attention of scientists since satellite images of the distribution of the global aerosols revealed that most of this aerosol is dust (Tegen and Fung, 1995). Moreover, the detection of dust is useful for tracking dust storms, which can limit the visibility of aircraft and inhibit all transportation. Blowing dust can be of great importance to the U.S. Department of Defense; for example, a dust storm caused the failure of the 1980 hostage rescue attempt in Iran. To estimate the effects of dust on climate and aviation, we first need to understand its optical and thermal properties.

Ground-based sensors are sparse, making it difficult to locate the origin of a dust storm or track its movement. This is the reason that satellite measurement is becoming popular in global dust detection. Since the main dust sources are desert and semi-desert regions, the brightness of the desert increases the difficulty of quantifying the amount of dust in the atmosphere in these areas; it is hoped that IR measurements can remedy this situation. IR techniques are applicable for both day and night. Techniques are needed to distinguish between lifted dust and sand left behind near and on the surface. Particle size becomes the main differentiator for dust and sand since in most cases the mineral composition of these two kinds of particles are similar. Here, we define dust as airborne sand above the planetary boundary layer ($> 2\text{ km}$) with diameters less than $10\text{ }\mu\text{m}$ and sand as desert particles below the top of the planetary boundary layer ($< 2\text{ km}$) with diameters larger than $10\text{ }\mu\text{m}$. The regional meteorological conditions play an important role in determining the vertical distributions of dust/sand. In our discussion, we assume that silicate is the major component of dust and sand.

Infrared-based techniques have been applied to both geostationary satellites (e.g., Shenk and Curran, 1974; Legrand *et al.*, 1989; Tanre *et al.*, 1988; Tanre and Legrand, 1991) and polar orbiting satellites (e.g., Ackerman, 1989, 1997) for detection of suspended particles in the atmosphere. The uniqueness for detection of atmospheric particles by using thermal measurements is that the techniques are applicable to high-albedo surfaces and at nighttime, where solar reflectance techniques usually fail. Early satellite IR techniques for dust storm detection were based on the 10.5-12.0 μm narrow band channel (Shenk and Curran, 1974). The IR narrow band has been found useful for detection of dust over land utilizing the bright temperature contrast between dust areas and the surrounding areas. However, the contrast was insufficient for dust detection over ocean. To overcome the difficulty of distinguishing the dust cloud from ice and water clouds associated with a single IR channel, the split window (11 μm and 12 μm) IR technique was introduced. It has been used to detect volcanic aerosols (such as Prata, 1989; Barton *et al.*, 1992) and dust outbreaks (e.g., Legrand *et al.*, 1989; Tanre and Legrand, 1991) based on brightness temperature difference between the two channels ($\text{BT}_{11}-\text{BT}_{12}$). Ackerman (1989) proposed using the brightness temperature difference between 3.7 μm and 11 μm to track dust outbreaks based on theoretical simulations. Recently, a tri-spectral technique, using the 8.3, 11, and 12.0 μm channels, has been proposed to detect volcanic aerosols over ocean (Ackerman and Strabala, 1994) and dust storms (Ackerman, 1997). The detection is based on brightness temperature differences among the three channels ($\text{BT}_{11}-\text{BT}_{12}$ and $\text{BT}_8-\text{BT}_{11}$).

The above IR techniques are based on the fact that aerosols display a strong spectral variation in the 8-9 μm and 10-12 μm regions. Moreover, the atmosphere is fairly transparent in these spectral regions. If the aerosol layer is optically thin, transmitted surface emissions are the major component of the measurement. If the aerosol layer is optically thick, aerosol emissions account for a major part of the measurement. For this reason, the 8-9 μm and 10-12 μm spectral regions are selected since gaseous absorption is weak but aerosol absorption is relatively strong. In practice, analysis is based on brightness temperature rather than radiance. The magnitude or sign of a brightness temperature difference versus the brightness temperature of one of the channels may imply the signature of aerosol loading.

Unfortunately, there are always some inconsistencies between theoretical model simulations and satellite observations. For example, negative differences in $\text{BT}_{11}-\text{BT}_{12}$ observed by satellite measurement during heavy dust loading cannot be obtained by a model simulation unless a specific dust aerosol model is assumed, which is not the case in reality. Moreover, complex surface emissivity may also complicate the radiative signal in some cases (such as volcanic aerosol detection over land) and make the aerosol detection difficult. Consequently, current IR techniques of aerosol detection are still qualitative.

Our dust detection algorithm will combine both visible and thermal techniques. The extended dark-pixel method developed by Kaufman *et al.* (1999) for visible blue and red channels (0.488 μm and 0.672 μm) will be used to detect dust in daytime. For nighttime detection, we propose to use four thermal bands (3.70 μm , 8.55 μm , 10.76 μm , and 12.01 μm) from VIIRS baseline channels to form a quad-spectral technique for dust detection. In a manner similar to the dust tracking technique proposed by Ackerman (1987) using the difference in brightness temperature between 3.70 μm and 10.76 μm bands, we will use three sets of differences in brightness temperature ($\text{BT}_{3.7}-\text{BT}_{8.55}$, $\text{BT}_{3.7}-\text{BT}_{10.8}$, and $\text{BT}_{3.7}-\text{BT}_{12.0}$) to form a dust index to represent the mass loading of dust storms. To separate lifted dust particles from the sand particles near the surface during the daytime and nighttime, the infrared spectral contrast technique proposed by Wald *et al.* (1998) can be used, which is based on strong differences between the thermal

properties of small dust particles (2-5 μm in diameter) and the large sand particles (> 70 μm in diameter) at two thermal channels (8.55 μm and 10.8 μm).

Our proposed nighttime detection technique will utilize the large difference between the dust refractive index between 3.7 μm band and the other three far IR bands (8.55, 10.8, and 12.0 μm) of the VIIRS instrument. The unique properties of the 3.7 band cause observable differences in the equivalent blackbody temperatures at these channels in the presence of a dust layer, thus providing a possibility to locate and track dust storms. In this section calculations using the MODTRAN radiation transfer model are performed to demonstrate the feasibility of using a quad-spectral technique to monitor dust storms over desert.

In the MODTRAN code, a desert aerosol model (Longtin *et al.*, 1988) with wind speed effect was chosen for radiation calculations of the dust storm. The desert aerosol model has a sand component consisting of quartz particles and quartz particles contaminated with a 10% concentration of hematite. Surface albedo (or emissivity) over desert are used in the calculations with a value of 0.4, 0.1, 0.05, 0.02 for 3.75, 8.3, 10.8, and 12.0 μm channels, respectively. These four channels are the baseline channels 10, Aerosol I, 11, and 12 of the VIIRS instrument. Figure 2 plots simulated brightness temperature at nighttime for the four channels versus turbidity (the aerosol optical thickness at 0.55 μm). The surface temperature T_s is 300°K. The calculation is performed at 20°N latitude, 350° longitude over the Sahara desert at night. The mid-latitude summer atmosphere in MODTRAN is used. We can see a very interesting feature—that is when desert aerosol loading increases— $BT_{3.75}-BT_{8.55}$, $BT_{3.75}-BT_{10.8}$, and $BT_{3.75}-BT_{12.0}$ will change sign from negative to positive. If this feature is robust for most atmospheric and surface conditions, then a dust storm index can be composed based on the sign of these brightness temperature differences corresponding to different aerosol loadings.

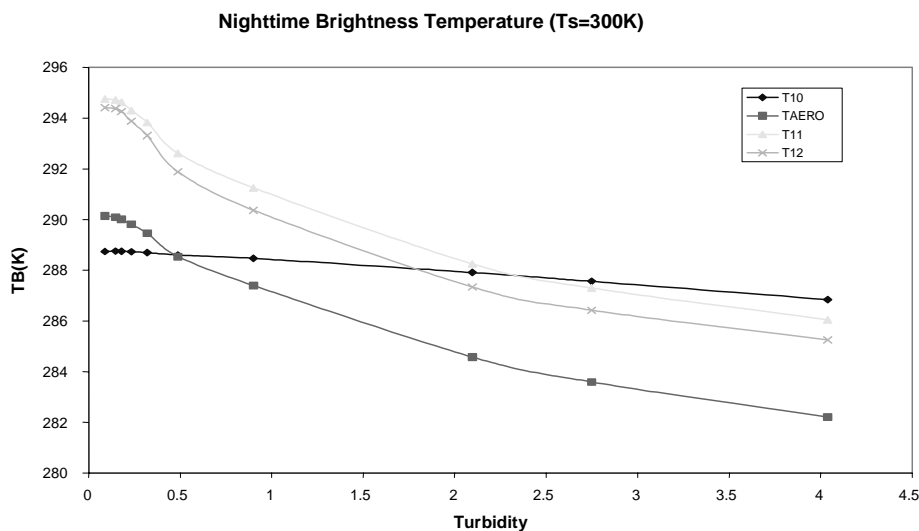


Figure 2. Nighttime brightness temperatures of VIIRS baseline channels 10 (T10), AERO 1 (TAERO), 11 (T11), and 12 (T12) versus turbidity.

We know that for a wavelength increase from 3.75 μm to 12.0 μm , the surface reflectance (or emission) decreases (or increases) very quickly over bright surfaces (e.g., over desert) as shown in Figure 3, which plots the reflectance in percentage versus wavelength for sand based on the MOSART database. Thus, the satellite measurement at these four channels for a thin aerosol layer is dominated by the contribution from the surface emission rather than by the atmospheric transmission features (this is not true for a dark surface like the ocean), which results in positive values of $\text{BT}_{3.75}-\text{BT}_{8.55}$, $\text{BT}_{3.75}-\text{BT}_{10.8}$, and $\text{BT}_{3.75}-\text{BT}_{12.0}$. When aerosol loading increases, surface emission contribution decreases quickly along with the increase of atmospheric thermal emission from the aerosol layer. This can be demonstrated by decomposing the TOA radiance (TOAR) into three components: contribution from (1) surface emission (CFSE), (2) atmospheric thermal emission (CFATE), and (3) surface reflected atmospheric thermal emission (CFSRATE). The mathematical expression of the relationship among these four quantities is $\text{TOAR}=\text{CFSE} + \text{CFATE} + \text{CFSRATE}$. Figures 4, 5, 6a, and 6b each plot, these four quantities versus turbidity for the case presented in Figure 2. We do see that CFSE decreases and CFATE increases when turbidity increases. CFSRATE increases at the beginning of turbidity increase but then starts to decrease monotonically when turbidity is large. This feature of CFSRATE is not important since its value is small compared to the other two quantities of the decomposition. Because the decrease of CFSE is faster than the increase of CFATE when turbidity increases, the net effect is a TOAR decrease slowly with turbidity increases because the compensation of CFSRATE (see Figure 7). We also notice that the features of variation of TOAR (or CFSE, CFATE, and CFSRATE) with turbidity in the four thermal bands are very similar. This implies that the relative changes of radiance caused by the change of aerosol loading in the four channels are almost the same, which is feasible from the physics.

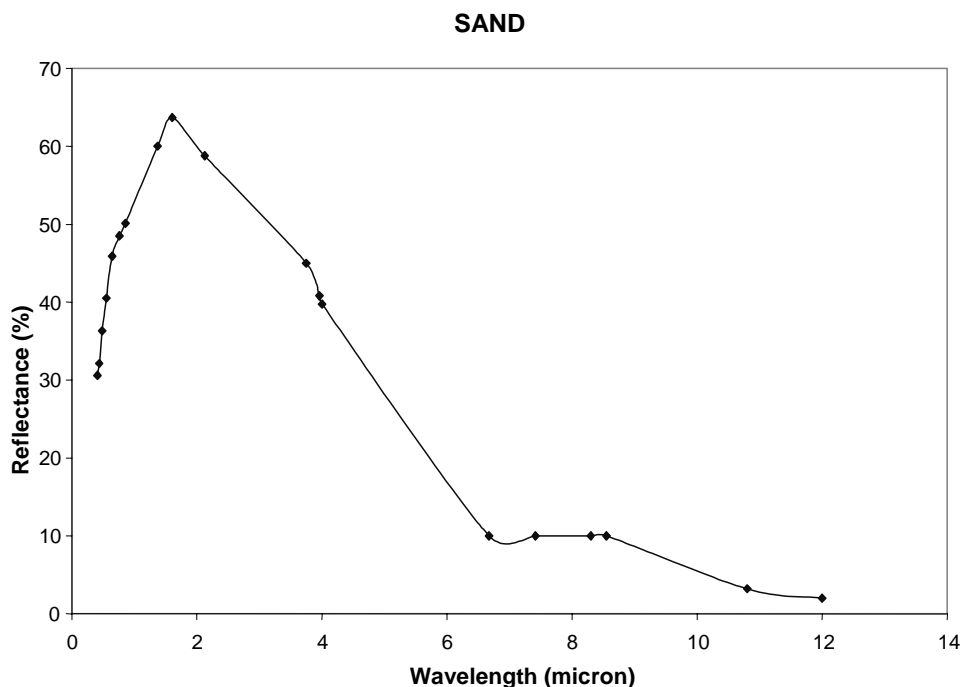


Figure 3. Spectral distribution of reflectance (%) over sand. The data is taken from the database of MOSART and interpolated to VIIRS bands.

Planck's Law states that variations in temperature are wavelength-dependent. To verify the nonlinear response, we selected the six radiances of the four channels (corresponding to a turbidity of about 0.9) in Figure 4 and added 10% variation to each. We then calculated the brightness temperatures corresponding to both the original radiances and the radiance with the 10% addition for the four channels along with the differences between the two brightness temperatures for each of the four channels. The results of temperature differences are $\Delta BT_{3.75} = -2.073K$, $\Delta BT_{8.55} = -4.512K$, $\Delta BT_{10.5} = -5.992K$, and $\Delta BT_{12.0} = -6.593K$. The brightness temperature decreases in the 8.55, 10.8, and 12.0 μm channels much faster than in the 3.75 μm channel. Sensitivity studies are included in the sensitivity study section that were performed to investigate whether the features observed in Figure 2 are robust enough for algorithm development.

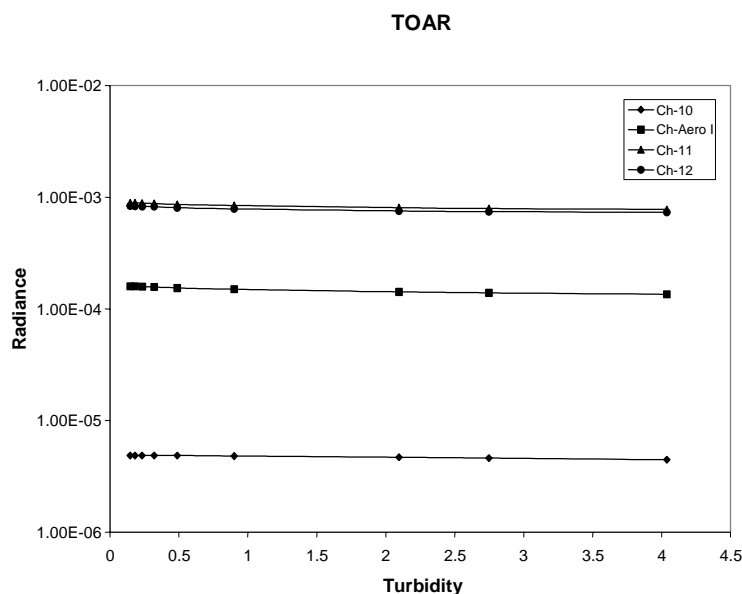


Figure 4. TOA radiance (TOAR) versus turbidity for VIIRS thermal bands for the case shown in Figure 2. The units of the radiance is ($Wcm^{-2} ster^{-1}$).

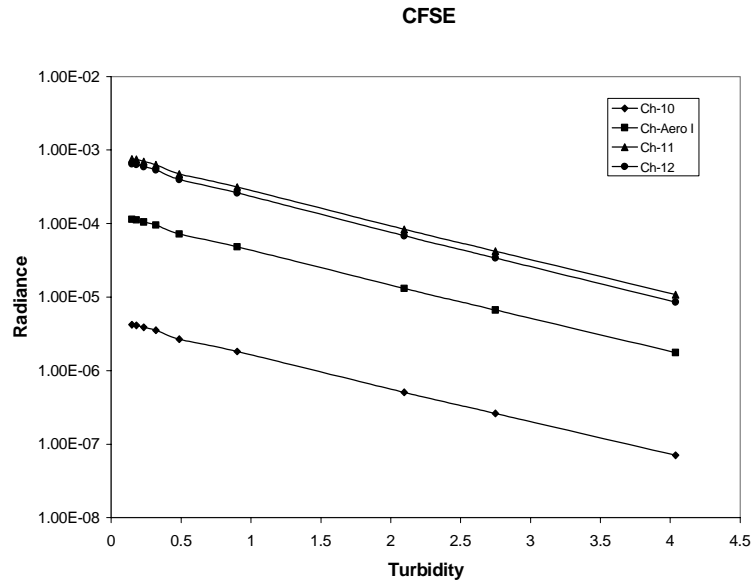


Figure 5. The contribution from surface emission (CFSE) versus the TOA radiance for VIIRS thermal bands for the case shown in Figure 2.

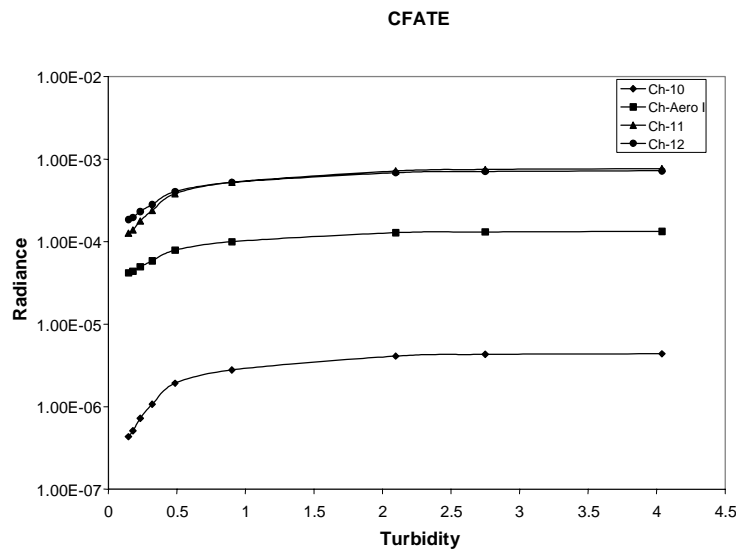


Figure 6a. The contribution from atmospheric thermal emission (CFATE) versus the TOA radiance for VIIRS thermal bands for the case shown in Figure 2.

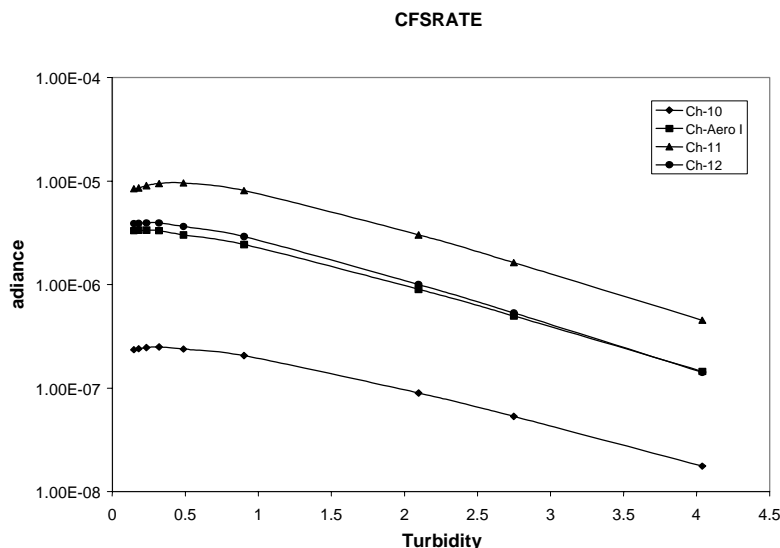


Figure 6b. The contribution from surface reflected atmospheric thermal emission (CFSRATE) versus the TOA radiance for VIIRS thermal bands for the case shown in Figure 2.

For daytime, the preferred method to detect dust is through the inversion of an aerosol model. However, strong events of dust/sand (or dust storm) can easily be interpreted as cloud by either the internal or external cloud mask, therefore we should have a-priori available a simple detection of such events. We are currently experimenting with the development of a heavy dust flag, for MODIS. The following figures illustrate the basic ideas and results on a particular case. Once again we rely on the spectral signature of the signal in the SWIR/MWIR region. Figure 7a shows a RGB composite of the corrected reflectance observed by MODIS for a dust storm (yellow-white) over the Mediterranean sea (left part of the image). Figure 7b shows the false RGB (SWIR/MWIR) composite; using this combination of wavelengths, we can also clearly discriminate the dust plume from the clouds. The plume appears more reddish than the white clouds. A simple test has been implemented to verify the spectral dependence in the SWIR/MWIR of the clouds detected by the internal cloud mask and restores the pixels that show a spectral dependence closer to the dust.

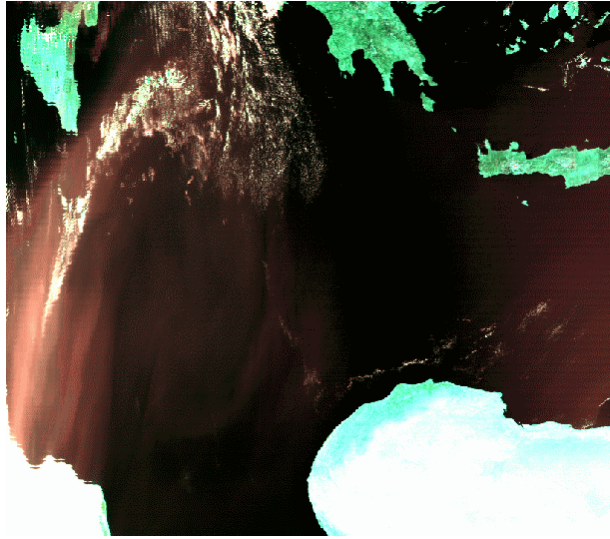


Figure 7a: RGB image (no aerosol correction) showing a dust storm (yellow-white) over the Mediterranean sea.

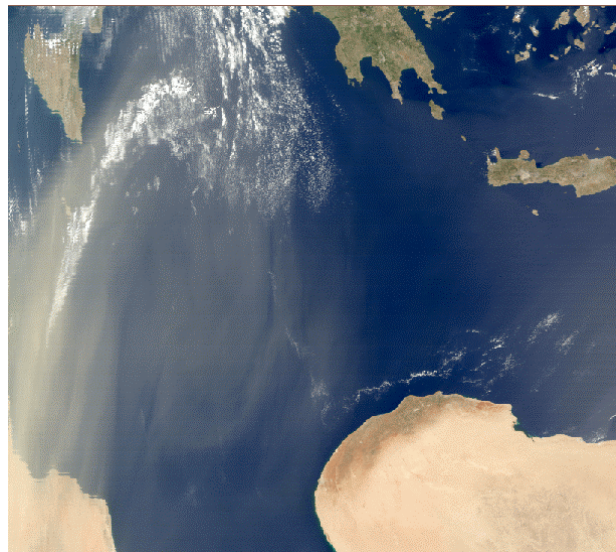


Figure 7b: False RGB image (2.1 μ m Blue, 1.6 μ m Green, 3.75 μ m Red), the low clouds appear whiter than the dust in this false RGB.



Figure 7c: Experimental dust storm mask. The area detected as strong dust concentration is colored in red-orange.

2.3.3 Sea Salt

Marine aerosols affect radiative transfer and climate directly by scattering and absorbing radiation and indirectly by influencing the droplet size distribution and albedo of marine boundary layer clouds. Thus, sea salt as a primary component of coarse marine aerosol particles plays an important role in radiative forcing.

Sea salt will be differentiated from the other types of suspended matter using size distribution and geographic location. Sea salt is composed primarily of sodium and chlorine and is injected into the atmosphere when air bubbles on the surface of the ocean burst in breaking waves. Sea salt has a unique size distribution that can be used to distinguish it from other possible suspended matter. Sea salt particles have an Angstrom exponent greater than 0.0 and less than 0.5, and the optical thickness is usually less than 0.15.

2.3.4 Smoke

Smoke detection is an important product for identifying areas of biomass burning. Part of the interest in smoke detection comes from its potential role in monitoring forest fires, which is a priority of the U.S. Department of Commerce. However, biomass burning is also important for the global environment due to the emission of trace gases and organic hygroscopic particles (Kaufman *et al.*, 1992). Some of the trace gases emitted are greenhouse gases (e.g., CO₂, CH₄, and CH₃Cl) that directly contribute to global warming. Others are chemically important in the troposphere (e.g., NO_x and CH₄) and are involved in reactions producing increased levels of ozone and acid precipitation. The organic particles introduced into the troposphere indirectly affect the radiation budget by altering cloud microphysics.

Smoke particles are small particles with an Angstrom exponent greater than 1.4 and exist at optical thicknesses greater than 0.5. Smoke also exhibits distinctive absorptive properties in the

visible bands. Our smoke detection module is inherited from the SeaWiFS smoke detection scheme developed by Eric Vermote, in which digital data (counts) are used as the input along with some ancillary data sets, including the sensor calibration data, land/water mask data, and surface elevation data. By combining these data sets with corrections for Rayleigh scattering and ozone, oxygen, and water vapor absorption, and by choosing a proper projection scheme, we can compose a global data set of reflectance for the 8 channels (412, 443, 490, 510, 550, 670, 765, and 865 nm) on SeaWiFS. These reflectances, aggregated to a resolution of 8 km by 8 km, are used to form a smoke index for smoke detection. This method has been proven successful with SeaWiFS data. Figure 2 shows smoke over Indonesia for April 10, 1998 as seen by SeaWiFS and the smoke detected by the Aerosol Index using TOMS data the same day.

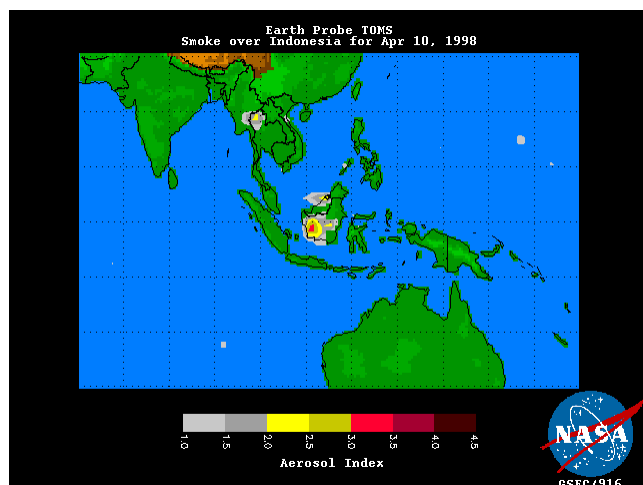
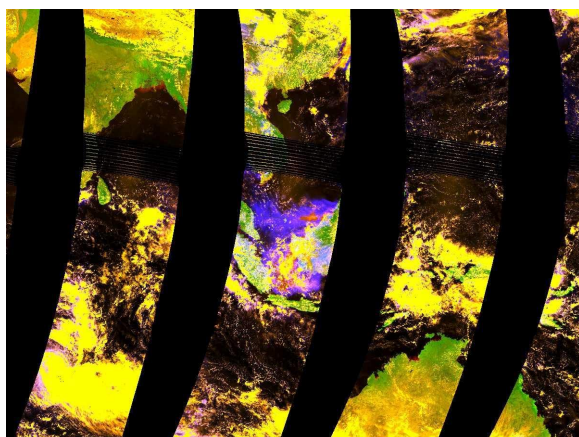


Figure 8. Top - Smoke over Indonesia for 10 April 1998 as seen by SeaWiFS. RGB composite, $R=0.67\mu\text{m}$, $G=0.87\mu\text{m}$, $B=\text{Smoke Index}$. Smoke is blue to violet as it is enhanced in the Blue and Red components. Bottom – TOMS Aerosol Index for the same day verifies the SeaWiFS detection of smoke.

The physical basis of the smoke index is that the SeaWiFS channel 1 (412 nm) reflectance (or radiance), ρ_1 , is sensitive to both smoke and cloud particles. While the reflectances of channels 2 (443 nm), 4 (510 nm), 5 (550 nm), 6 (670 nm), are uniform ($\rho_2 - \rho_4 \approx 0$; $\rho_5 - \rho_6 \approx 0$) for clouds but different ($\rho_2 - \rho_4 > 0$; $\rho_5 - \rho_6 > 0$) for smoke. Thus, the combination, $\rho_1 \times (\rho_2 - \rho_4) \times (\rho_5 - \rho_6) \times 10000$, is close to zero for clouds but much larger than zero for smoke, creating a smoke index. Because the VIIRS channels are close to those of SeaWiFS, the SeaWiFS smoke detection scheme should be applicable to VIIRS without much modification. This will be the primary test for smoke detection (Smoke I).

A second test for smoke (Smoke II) will be performed. This test will use typical properties of smoke cover with regard to optical thickness and size parameter (which are the products of aerosol retrieval), as well as geolocation, to detect smoke.

In addition to detecting smoke, its concentration will also be found using two methods described in Section 3.3.11. These methods use the smoke index, the aerosol optical thickness at 550 nm, and the reflectance at 670 nm as inputs. The output is smoke concentration along the line of sight in $\mu\text{g}/\text{m}^3$.

3.0 ALGORITHM DESCRIPTION

3.1 PROCESSING OUTLINE

The data flow chart presented here is the eventual goal of the suspended matter algorithm, though the diagram will evolve as the algorithm develops. The data flow chart presented in Figure 8 illustrates the anticipated processing procedures.

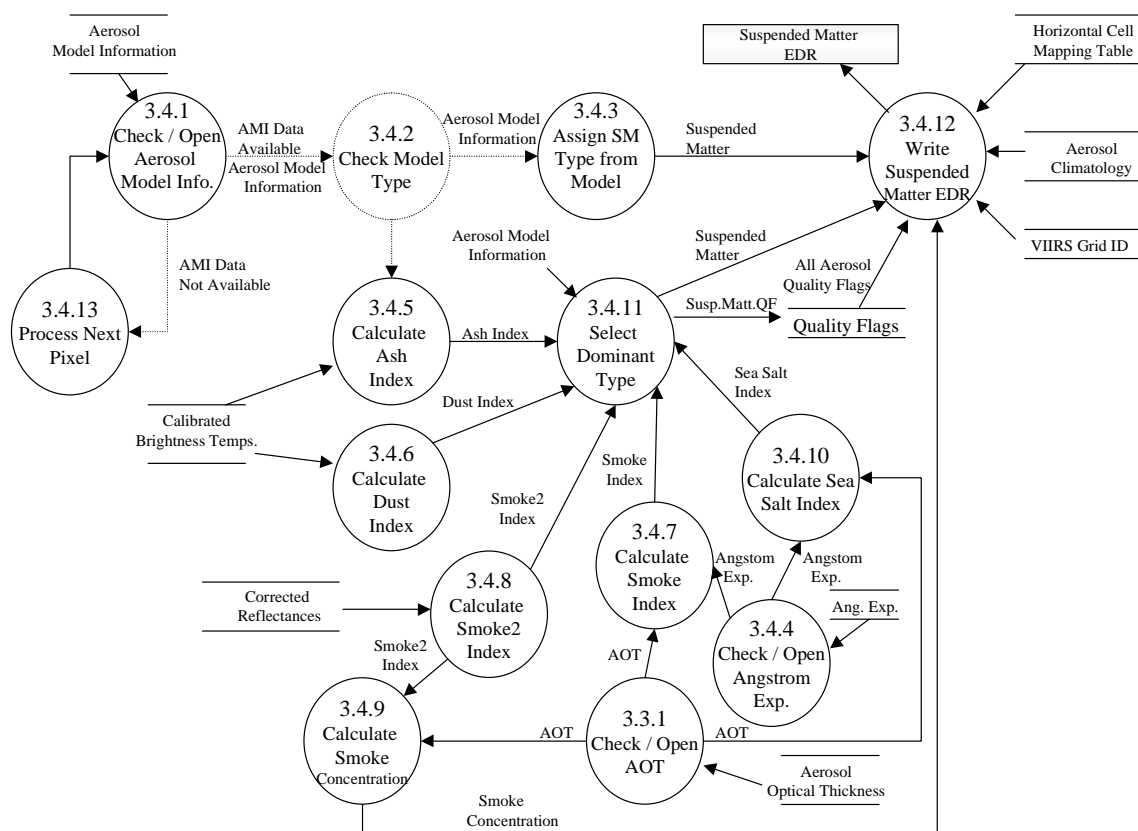


Figure 9. Suspended Matter Data Flow Diagram.

3.2 ALGORITHM INPUT

The algorithm requires ancillary information from the VIIRS instrument and from outside sources. Much of the non-VIIRS data can be obtained from the other instruments on NPOESS. Because the capability to detect suspended matter will be a by-product of other EDRs (e.g., aerosol optical thickness), the required accuracy of the ancillary data should be the same accuracy required for those EDRs.

3.2.1 VIIRS Data

The VIIRS data required by the suspended matter algorithm are higher-level VIIRS products and are summarized in Table 2.

Table 3. VIIRS data required by the suspended matter algorithm

Input Data	Source of Data
Cloud Information	VIIRS Cloud Mask
Land/Water Information	VIIRS Cloud Mask
VIIRS Calibrated Reflectances	VIIRS 750m Earth View SDR
VIIRS Calibrated Brightness Temperatures	VIIRS 750m Earth View SDR
Aerosol Optical Depth	VIIRS Aerosol Optical Thickness IP
Aerosol Particle Size Parameter	VIIRS Angstrom Exponent IP

3.2.1.1 Cloud Mask

The suspended matter EDR is only required for clear, or cloud-free, conditions, and some types of suspended matter, such as dust/sand, and sea salt, can only be detected in clear conditions. Thus, a cloud mask to remove pixels contaminated by cloud cover is needed. A pixel is considered cloudy for the purposes of this EDR if the VIIRS cloud mask indicates a cloudy pixel.

3.2.1.2 Land/Water Mask

The algorithm for determining the aerosol optical thickness uses two different procedures depending on whether the pixel is over land or over water. This information is needed to help identify the type of suspended matter. Even for thermal bands, some of our techniques for the detection of suspended matter (e.g., volcanic ash and dust) are applicable either only over ocean or only over land. This information will probably be included in the packet of information received from the cloud mask.

3.2.1.3 Calibrated TOA Reflectances and Brightness Temperatures

The VIIRS-observed calibrated reflectances and brightness temperatures are required for detection of volcanic ash, dust/sand, and smoke.

3.2.1.4 Aerosol Optical Thickness IP

The suspended matter algorithm will use the Aerosol Optical Thickness IP to distinguish some types of suspended matter, such as smoke and dust in daytime. The Aerosol Optical Thickness IP

will be produced immediately preceding the Suspended Matter EDR, and thus the optical thickness output will be input directly into the suspended matter algorithm.

3.2.1.5 Angstrom Exponent IP

The suspended matter algorithm will use the Angstrom Exponent to distinguish some types of suspended matter, such as sea salt. The Angstrom Exponent IP will be produced immediately preceding the Suspended Matter EDR, and thus the angstrom exponent output will be input directly into the suspended matter algorithm.

3.2.2 Non-VIIRS Data

There is no non-VIIRS data required by the suspended matter algorithm. The Aerosol Index as calculated from OMPS data may provide enhanced performance of the algorithm.

Table 4. Non-VIIRS data required by the suspended matter algorithm

Input Data	Source of Data
Aerosol Index	OMPS Calibrated Reflectance SDR

3.2.2.1 Aerosol Index

An aerosol index produced from the 340 and 380 nm channels of OMPS on NPOESS can be used to help differentiate suspended matter and calculate the aerosol optical thickness and size parameter, as absorption is one of the largest uncertainties in this retrieval. This product may also aid in determining the vertical distribution of suspended matter. The radiances as measured by OMPS are the only data required for this index. Work performed by the Aerosol IPT has shown the Absorbing Index to be very helpful in determining the presence of dust in desert regions and smoke in vegetated regions. However, the final decision on whether to use this information and how to use it are still under investigation.

3.3 THEORETICAL DESCRIPTION OF SUSPENDED MATTER RETRIEVALS

3.3.1 Quality Check of the Input Data

3.3.1.1 Physics of the Problem

The suspended matter retrieval is only required for clear conditions, yet smoke, ash and dust may be mistaken for clouds by the cloud mask. The suspended matter algorithm will use the spectral detection methods over all pixels. The aerosol optical thickness and particle size parameter are only retrieved for non-cloudy areas, and thus the differentiation of type using this information will only be available for non-cloudy areas. A cloud mask will provide cloud cover information. The Earth's surface type for a given pixel must also be determined, as different processes are used for aerosol retrieval over land and over water.

3.3.1.2 Mathematical Description of the Algorithm

A quality control flag in the input image data is used to separate land from ocean and to identify the usability of each pixel. The quality control flag consists of 8 bits. Bit 0 tells us whether that particular pixel is a mixed pixel, meaning partially cloudy. Bit 1 indicates whether this is a cloudy pixel. The algorithm does not compute the data product for cloudy pixels. Bit 2 indicates whether the pixel is covered by cloud shadow. Bit 3 gives the land/ocean mask information. If bit 3 is 1, then the location is over ocean; if bit 3 is 0, then the location is over land. Bit 4 indicates sun glint over the ocean, and bit 7 gives the information as to whether this is a valid observation and can be used for retrieval. A loop iterates over every pixel in the input data. If the pixel is labeled as a valid observation, meaning that it meets all of the necessary criteria mentioned above, then the process continues on. If the pixel fails the quality control test, then it is discarded and the next pixel is considered. The Suspended Matter Algorithm does not use bits 5 and 6.

3.3.2 Cloud Check

Aerosol and suspended matter EDRs are only required for cloud-free conditions. Thus, a cloud mask to remove pixels contaminated by cloud cover is necessary for channels located within the visible region. For the thermal band technique, the cloud mask is not essential.

3.3.3 Land/Water Check

Information on the location (land or water) of the pixel is needed to apply different algorithms over land and water. This information will be supplied in the cloud mask information.

3.3.4 Volcanic Ash Detection Module

The algorithm will implement the GOES technique for volcanic ash detection (see section 2.3.1). This method uses a combination of three near-infrared (NIR) bands—4.0 μm , 10.7 μm , and 12.0 μm —to differentiate between meteorological (ice and water) clouds and volcanic ash clouds. Immediately after an eruption, the ash cloud is opaque. At this time, the ash cloud is indistinguishable from a meteorological cloud. After a few hours, the volcanic ash cloud thins and the properties of the sulfuric acid within the ash cloud enable the cloud to be distinguishable from a meteorological cloud.

For a transparent meteorological cloud, the cloud absorbs more energy from the surface at 12.0 μm than at 10.7 μm due to the higher refractive indices for water ice particles at 12.0 μm than at 10.7 μm . A positive difference is created when the brightness temperature of the 12.0 μm band is subtracted from the brightness temperature of the 10.7 μm band. In a transparent volcanic ash cloud, the absorption of energy from the underlying surface is greater at 10.7 μm than at 12.0 μm due to the larger refractive index for silicates at 10.7 μm than at 12.0 μm . Here, a negative difference is created when $BT_{12.0}$ is subtracted from $BT_{10.7}$. This difference product is used to create a “Split Window” image that shows the location of the volcanic ash cloud.

The 4.0 μm band is used to further enhance the location of the ash cloud by creating a brightness temperature difference image from the 4.0 μm and 10.7 μm bands. Ash is warmer in the 4.0 μm band than in the 10.7 μm band due to daytime reflectance and to strong emittance anytime due to

SO₂ in the 4.0 μm band. The two images produced above are combined. Volcanic ash will stand out against clouds immediately after a strong eruption because of the greater warmth of the ash. When the ash thins, it is more difficult to detect. The 4.0 band is also sensitive to “hot spots,” or very hot land surfaces. Active volcanoes will appear as white spots on the 4.0 μm band image in cloudless conditions. The 1.38 μm band can be used to detect ash that has been injected into the stratosphere.

3.3.5 Dust/Sand Detection Module

Dust, or sand, detection is based on brightness temperature differences among three IR channels (8.55 μm , 10.8 μm , and 12.0 μm) $\text{BT}_{8.55}-\text{BT}_{10.8}$ and $\text{BT}_{10.8}-\text{BT}_{12.0}$ (Ackerman, 1997; Wald *et al.*, 1998). Negative differences in $\text{BT}_{10.8}-\text{BT}_{12}$ are useful for detecting and tracking dust storms. These three IR channels are also useful for detecting stratospheric volcanic aerosols over oceans. We are now investigating the potential addition of channel 10 (3.75 μm) for developing an operational dust storm detection technique at night.

Figure 2 plots MODTRAN simulated brightness temperature ($\text{BT}_{3.75}$, $\text{BT}_{8.55}$, $\text{BT}_{10.8}$, $\text{BT}_{12.0}$) at nighttime for the four channels (3.75 μm , 8.55 μm , 10.8 μm , and 12.0 μm) respectively versus turbidity (the aerosol optical thickness at 0.55 μm). The surface temperature (T_s) is 300 K. The calculation is performed at 20°N latitude, 350° longitude over the Sahara desert. We can see a very interesting feature—that is, when desert loading increases, $\text{BT}_{3.75}-\text{BT}_{8.55}$, $\text{BT}_{3.75}-\text{BT}_{10.8}$, and $\text{BT}_{3.75}-\text{BT}_{12.0}$ will change sign from negative to positive. We have performed tests and found this feature robust for most atmospheric and surface conditions. We will composite a dust storm index based on the sign of these three brightness temperature differences to signify the dust loading.

3.3.6 Sea Salt Detection Module

Sea salt will be differentiated from the other types of suspended matter using size distribution and geographic location. This method will only be applicable over the ocean, as Effective Radius from the Aerosol Particle Size Parameter EDR will not be available over land. Sea salt is composed primarily of sodium and chlorine and is injected into the atmosphere when air bubbles on the surface of the ocean burst in breaking waves. Sea salt has unique size properties that can be used to distinguish it from other possible suspended matter. The Angstrom exponent of sea salt is greater than 0.0 and less than 0.5 and the optical thickness is usually less than 0.15.

3.3.7 Smoke Detection Module

A smoke index generated in our Smoke Detection Module will be used to identify smoke in the view field of the sensor. The physical basis is that reflectance (or radiance), $\rho_{0.413}$, near 0.413 μm is sensitive to both smoke and cloud particles. The reflectances near 0.443 μm , $\rho_{0.443}$, and 0.488 μm , $\rho_{0.488}$, are uniform ($\rho_{0.443}-\rho_{0.488}\approx 0$) for clouds, which is also true ($\rho_{0.556}-\rho_{0.645}\approx 0$) for reflectance near 0.550 μm , $\rho_{0.556}$, and 0.670 μm , $\rho_{0.645}$. However, as $\rho_{0.443}-\rho_{0.488}>0$ and $\rho_{0.556}-\rho_{0.645}>0$ for smoke, the composition $\rho_{0.413} \times (\rho_{0.443}-\rho_{0.488}) \times (\rho_{0.556}-\rho_{0.645}) \times 10000$ is close to zero for clouds but much larger than zero for smoke. Thus, it is used as a smoke index in our algorithm.

3.3.8 Second Smoke Detection Module

A second test for smoke detection will be performed after all other tests to check for smoke not detected through the first smoke detection module. This second method of smoke detection will use the optical thickness and size parameter of the aerosol to identify it as smoke. If the Angstrom exponent is greater than 1.5 and the aerosol optical thickness is greater than one (TBD), then smoke can be defined to be present, provided it is confirmed by a positive value of the smoke index.

3.3.9 Smoke Concentration

One of the objective requirements in the VIIRS SRD is to measure smoke concentration in micrograms per cubic meter ($\mu\text{g}/\text{m}^3$). In this section we describe two methods of achieving this goal. The initial accuracy is expected to be of the order of 50% for these methods, but can potentially be improved with more surface measurements and with additional theoretical and experimental work. These techniques for deriving smoke concentration are only valid over dark surfaces where aerosol optical depths can be derived.

3.3.9.1 Use of Aerosol Optical Thickness Measurements

A number of studies (d'Almeida et al., 1991) have shown that aerosol concentration C can be related to visibility (V). In general, the concentration is inversely proportional to visibility and according to the Auburn University Private Forest Management Team, can be expressed as follows:

$$C = 1000/V \quad (1)$$

where V is the visibility in kilometers and C is the smoke concentration in $\mu\text{g}/\text{m}^3$. This approximate expression is accurate to about 50% and needs to be refined. The visibility is horizontal visibility and VIIRS is responding to vertical visibility, so there probably will be no one expression that is always applicable due to the complex structure associated with smoke plumes.

Visibility can also be related to aerosol optical thickness. From Iqbal (1983) the relationship for low visibilities can be written as:

$$V = 3.9449 / (\beta/0.55^\alpha - 0.08498) \quad (2)$$

where α and β are the Angstrom coefficients, V is the visibility in kilometers, and 0.55 is the wavelength at which visibility is measured, namely 0.55 microns (or 550nm).

The previous expression can be written in terms of the aerosol optical thickness at 550 nm (τ_{550}) as follows:

$$V = 3.9449 / (\tau_{550} - 0.08498) \quad (3)$$

This form is advantageous for VIIRS since it measures τ_{550} directly with a band at 555 nm. Thus, in this formulation it is not required to use multiple bands to get the Angstrom coefficients. Rather a single band can be used, making the measurements much simpler.

The first and third equations above can be combined to give the smoke concentration C as follows:

$$C = 253.5 \tau_{550} - 21.5 \quad (4)$$

A plot of this relationship is shown in Figure 10:

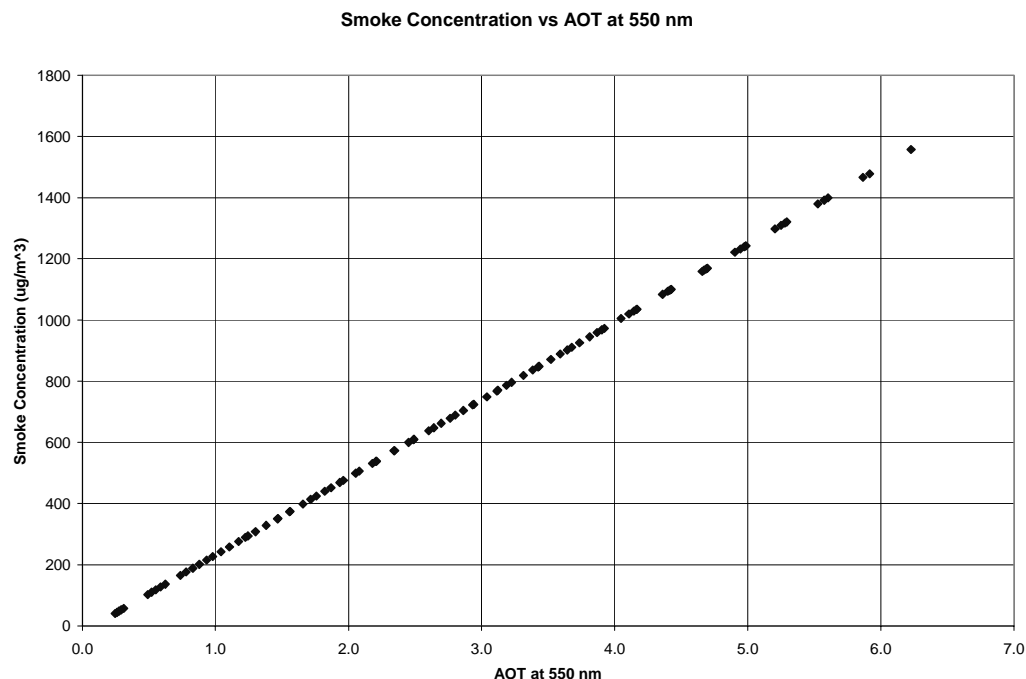


Figure 10. Smoke concentration ($\mu\text{g}/\text{m}^3$) vs aerosol optical thickness at 550 nm.

As mentioned above this approach is expected to be accurate to within about 50% because of limitations on the accuracy of relating visibility to smoke concentration.

3.3.9.2 Use of VIIRS Smoke Index (SI)

There is an alternative approach to determining smoke concentration that has both advantages and disadvantages compared to the AOT approach. For VIIRS, a Smoke Index (SI) has been designed specifically to detect the presence of smoke. It is defined as follows:

$$SI = 10000\rho_{413}(\rho_{443} - \rho_{488})(\rho_{556} - \rho_{670}) \quad (5)$$

Where the ρ 's are reflectances for 5 different bands of VIIRS. SI is designed so that for clouds it will be near zero, but for smoke it will be much greater than zero. SI takes advantage of the fact that smoke has a strong spectral dependence in its reflectance because it consists of many small particles.

Using the 6S radiative transfer code (Vermote et al., 1997), values of the Smoke Index were simulated for a large number of viewing and illumination geometries for optical depths of 1, 2, 3, 4, and 5 at 550 nm. The biomass aerosol was used to simulate smoke and it has an Angstrom exponent of 1.5. The results of this simulation are plotted in Figure 11:

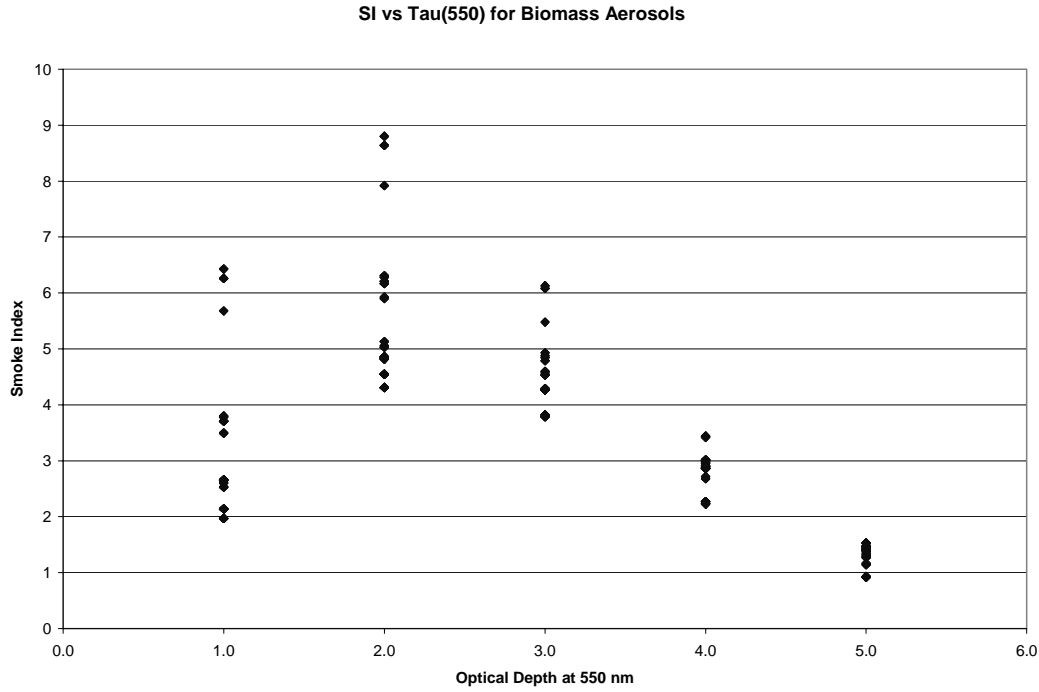


Figure 11. The Smoke Index simulated using the 6S radiative transfer code versus the aerosol optical depth at 550 nm.

From Figure 11, we see the Smoke Index increases until about an optical depth of 2 and then decreases. The lower values at higher optical depths are attributable to the absorbing properties of smoke. At low optical depths, smoke appears white. As it gets thicker it turns gray and eventually black. Consequently one gets lower values for the Smoke Index at higher optical depths as shown in the plot.

The scatter in the values is attributable to different viewing and illumination geometries. Ignoring these secondary variations, it is possible to get a fit of the Smoke Index (SI) as a function of optical depth at 550 nm (τ) as follows:

$$SI = -0.00108\tau + 5.867\tau^2 - 3.605\tau^3 + 0.767\tau^4 - 0.0558\tau^5 \quad (6)$$

This equation explains about 75% of the variance in SI and reproduces their value to an accuracy of about 25% (one sigma). It is derived using 21,124 combinations of viewing and illumination geometries and aerosol optical thicknesses.

From equation 6 and from Figure 11, it is evident that for a given value of SI, two possible values for aerosol optical depth exist. Thus, for a given Smoke Index, two values of smoke concentration can be derived. This lack of a unique answer reduces the usefulness of the Smoke Index as an independent parameter to derive smoke concentration. Using equations 4 and 6, we provide a plot of smoke concentration versus Smoke Index in Figure 12.

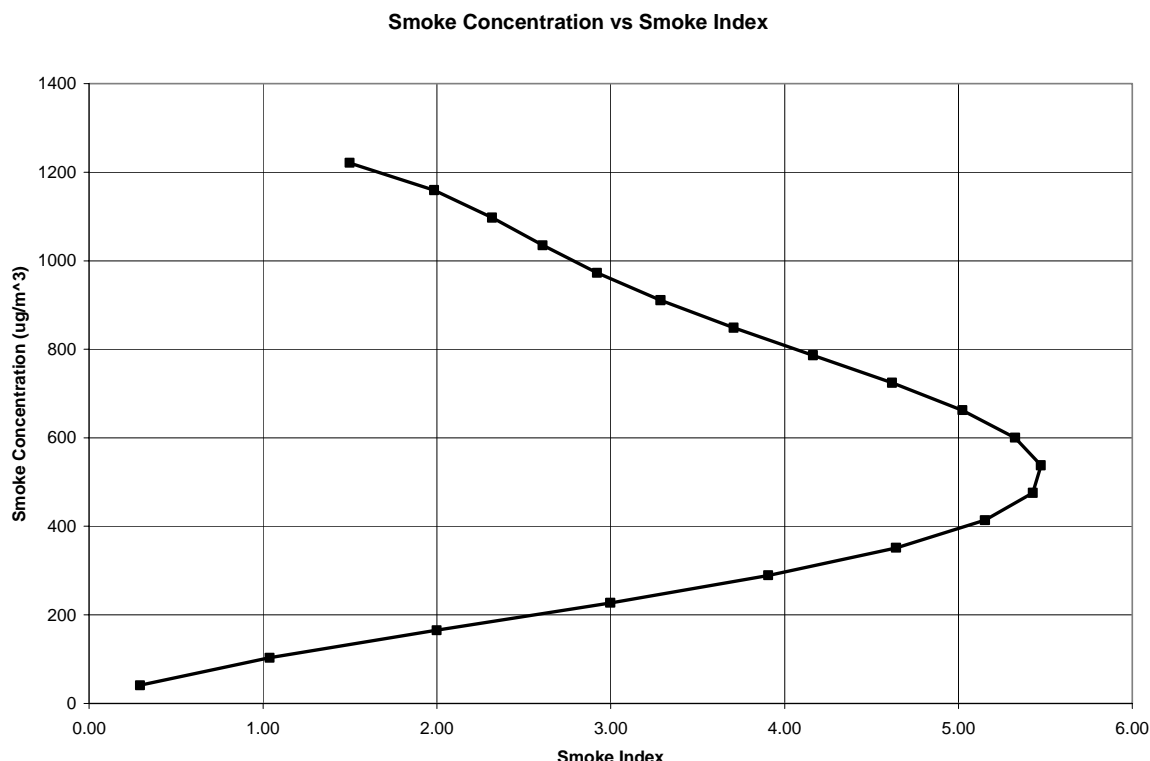


Figure 12. Smoke concentration versus the Smoke Index. Note that two possible smoke concentrations exist for each value of the Smoke Index.

In most cases we expect smoke to be white and thus we expect most observations of smoke will be along the lower portion of the curve in Figure 12. If this assumption is true, the smoke concentration can be expressed in terms of the Smoke Index (SI) as follows:

$$C = 21.4 + 72.96 \cdot SI \quad (7)$$

where this regression equation accounts for 99.7% of the variance for smoke concentrations less than $350 \mu\text{g}/\text{m}^3$. Equation 7 works well when the reflectance of band 5 (ρ_{670}) is less than 0.2. For $\rho_{670} > 0.2$, the following formula provides a good measure of smoke concentration:

$$C = -1258.6 + 8383.3 \cdot \rho_{670} \quad (8)$$

Equation 8 accounts for 98% of the variance for cases where the smoke concentration is greater than $350 \mu\text{g}/\text{m}^3$. Using equation 7 when $\rho_{670} < 0.2$ and equation 8 when $\rho_{670} > 0.2$, for those cases where the Smoke Index indicates smoke is present, allows the smoke concentration to be found to within an accuracy of about 10% in most cases, although a more thorough error analysis is still required.

3.3.9.3 Conclusions

Two approaches to obtaining smoke concentration have been described and may be called the AOT and SI approaches respectively.

The AOT approach is simple and requires only one measurement band. Its accuracy, however, is only about 50% and it will probably not work well for high smoke concentrations since the AOT values are more uncertain there. The Smoke Index may be used to identify regions where smoke exists, and then the AOT technique could be applied to derive smoke concentration.

The SI approach requires the use of 5 measurement bands. Because smoke is absorbing, the Smoke Index first rises for low concentrations and then falls as absorption becomes dominant for thick smoke. The result is that there are two possible aerosol thickness values for each Smoke Index value. This lack of a single value means that a unique smoke concentration value cannot be derived from the Smoke Index alone. If the observations are further broken into two categories based upon the reflectance of band 5 being less than or greater than 0.2, it is possible to derive two equations to get unique values for the smoke concentration

Ground-based observers will measure smoke concentration along horizontal paths. VIIRS will measure along roughly vertical paths. Because of this difference in measuring geometry, it will be difficult to validate the smoke concentrations derived from any satellite sensor.

The algorithms to get smoke concentration (C) can be summarized as follows:

1. If the Smoke Index (SI) is greater than one, then:

$$C = 253.5 \tau_{550} - 21.5 \quad (9)$$

- 2a. Alternatively, if SI is greater than one and ρ_{670} is less than 0.2, then:

$$C = 21.4 + 72.96 * SI \quad (10)$$

- 2b. If SI is greater than one and ρ_{670} is greater than 0.2, then:

$$C = -1258.6 + 8383.3 * \rho_{670} \quad (11)$$

In summary, two techniques can be used to meet the SRD objective of obtaining a measurement of smoke concentration. Method 1 is the simplest and the preferred method for deriving smoke concentration. Similar procedures can be use to derive concentrations for other aerosol types.

3.3.10 Aerosol Types and Aerosol Optical Properties

The primary discriminator for aerosol types is the Angstrom size parameter (α). Secondary discriminators are aerosol optical depth and the Smoke Index (SI). These parameters are chosen because VIIRS will derive them and they are consistent with WMO and other compilations of aerosol types. The table below summarizes the proposed suspended matter classification for tropospheric aerosols:

Table 5. Proposed aerosol type classification scheme for aerosols using the Angstrom coefficients and Smoke Index (SI) as inputs.

Aerosol Type	Optical Properties
Desert aerosols (dust/sand)	$\alpha < 0.0$ (all τ)
Desert aerosols (dust/sand)	$0.0 < \alpha < 0.5$ ($\tau > 0.25$)
Mixed (desert/maritime)	$0.0 < \alpha < 0.5$ ($0.15 < \tau < 0.25$)
Maritime aerosols (sea salt)	$0.0 < \alpha < 0.5$ ($\tau < 0.15$)
Mixed (maritime/continental)	$0.5 < \alpha < 0.8$ (all τ)
Continental aerosols	$0.8 < \alpha < 1.4$ (all τ)
Continental aerosols	$\alpha > 1.4$ (if smoke index SI < 0)
Smoke	$\alpha > 1.4$ (if SI > 0 & $\tau > 0.5$)
Volcanic ash	(Use IR signature)

The aerosol type classification scheme above was developed based upon the WMO aerosol classification type, d'Almeida's aerosol types, and other literature sources. A summary of aerosol types as a function of the Angstrom exponent, as given in the literature, is summarized in the table below.

The 6S radiative transfer code aerosol types are WMO-112. The LOWTRAN and MODTRAN aerosol types are identical to each other. Since desert and maritime aerosols have nearly the same α values, they are further distinguished based upon optical depth with low optical depths being associated with maritime aerosols and high values with desert aerosols. Intermediate optical depths are assumed to be a mix of the two types. The listed cutoff values in optical depth need to be refined based upon observations.

Continental aerosols are chosen to have range of α from 0.8 to 1.4 or 1.1 ± 0.3 (i.e., symmetrically distributed about 1.1). Aerosols with $\alpha > 1.4$ are taken to be continental unless the smoke index identifies them as smoke. The Canadian smoke data comes from O'Neill et al. (May 29, 1999 seminar).

Table 6. Aerosol types as a function of Angstrom exponent.

Aerosol Type	α
Desert wind-carried (d'Almeida)	-0.063
Desert background (d'Almeida)	0.058
Desert (6S code; WMO-112)	0.337
Clean maritime (d'Almeida)	0.114
Maritime (WMO-112)	0.252
Maritime (LOWTRAN)	0.499
Maritime/polluted (d'Almeida)	0.713
Clean continental (d'Almeida)	1.048
Average continental (d'Almeida)	1.142
Continental (WMO-112)	1.082
Rural (LOWTRAN)	1.073
Urban (d'Almeida)	1.152
Urban/industrial (WMO-112)	1.233
Urban (LOWTRAN)	0.941
Biomass smoke (6S code; WMO-112)	1.503
Smoke (Canadian forest fires)	1.700
Volcanic 1 (WCP-55)	-0.029
Volcanic 2 (WMO-112)	0.495

The aerosol type classification scheme proposed here will be refined and used in the algorithm to help meet the SRD objectives for suspended matter.

3.3.11 EDR Requirements

The requirements that must be fulfilled by the algorithm are defined in the System Specification (Table 4) published by the Integrated Program Office (IPO).

Table 7. Suspended Matter System Specification Requirements.

Requirement Number	Parameter	Requirement
SSV0178	EDR SUSMAT HCS:	1.6 km
SSV0179	EDR SUSMAT HRI :	HCS
SSV0180	EDR SUSMAT Vertical Cell Size	Total Column
SSV0182	EDR SUSMAT Horizontal Coverage	Global
SSV0184	EDR SUSMAT Probability of Detection, Suspended Matter	90%
SSV0185	EDR SUSMAT Probability of Correct Typing, Dust/sand present	85%
SSV0743	EDR SUSMAT Probability of Correct Typing, Smoke present	85%
SSV0744	EDR SUSMAT Probability of Correct Typing, Volcanic ash present	85%
SSV0745	EDR SUSMAT Probability of Correct Typing, Sea Salt present	85%
SSV0746	EDR SUSMAT Smoke Concentration Measurement Range:	0 to 1000 $\mu\text{g}/\text{m}^3$
SSV0187	EDR SUSMAT Smoke Concentration Measurement Uncertainty:	50%
SSV0189	EDR SUSMAT Swath Width	3000 km

3.3.12 Error Budget

The accuracy of this algorithm is determined by all of the errors affecting the final product. There are no explicit detectability requirements for the types of suspended matter of interest. The capability to detect suspended matter will be a by-product of the capabilities required by other EDRs. Thus, the error tolerance for this EDR is less confined than that of other aerosol EDRs, such as optical thickness and size parameter.

The possible major sources of error include uncertainties in the surface reflectance and in the aerosol model involved, instrument calibration error, geolocation mapping error, and errors in ancillary data. These errors are discussed within the Aerosol Error Budgets [V-3].

3.4 ALGORITHM SENSITIVITY STUDIES

3.4.1 Ash Detection Module

MODTRAN was used for preliminary simulations of ash and meteorological clouds to test the band subtraction technique. MODTRAN was chosen for use because of its easily applied volcanic ash models of differing vertical distribution of ash and extinction models, as well as its cirrus and cumulus cloud models. Various simulations were completed to show the dependence of the derived ash index on the angle between the sensor and the sun, and for the ocean with a maritime extinction model and forest with a rural extinction model.

The MODTRAN simulations differed only in the type of cloud simulated and in the albedo and aerosol and atmospheric models. A tropical model atmosphere was assumed with a vertical or

slant atmospheric path between two altitudes, and the program was run in radiance mode with multiple scattering. The boundary temperature used was 300 K. Ocean and forest albedos were used for the ocean and land simulations respectively. The ocean case used a maritime extinction with visibility of 23 km, and the land case used a rural extinction with visibility of 5 km. The DISORT algorithm was used with 8 streams. The season, spring-summer, was determined by the model. The initial altitude used was that of the proposed VIIRS, 833km. The final altitude differed depending on the type of cloud simulated. The angle between the sensor and the sun was varied, and the latitude and longitude chosen were in the Atlantic. The bands simulated were bands M15 and M16 of the VIIRS baseline, 10.3 to 11.3 μm and 11.5 to 12.5 μm respectively.

To simulate the ash cloud, the MODTRAN volcanic models were used. The models vary with vertical distribution and extinction model as shown in Table 5.

Table 8. MODTRAN Volcanic Models for Different Vertical Distributions and Extinction Models

Extinction Model	Vertical Distribution			
	Background Stratospheric	Moderate Volcanic	High Volcanic	Extreme Volcanic
Background Stratospheric	0,1	6	7	-
Aged Volcanic	-	2	4	-
Fresh Volcanic	-	5	3	8

No other type of cloud was assumed and simulations were run for each distribution/extinction model combination. A cloud height of 20 km was assumed for the ash cloud. The standard cirrus and cumulus models were assumed separately with cloud heights of 18 km and 5 km respectively. Background stratospheric models were assumed for the meteorological cloud simulations.

The brightness temperatures were calculated and the brightness temperature of band 12 ($BT_{12.0}$) was subtracted from that of band 11 ($BT_{10.8}$).

Figures 13 and 14 illustrate the derived ash indices ($BT_{10.8}-BT_{12.0}$) for the land and ocean cases described above.

Figure 13 illustrates the relative azimuth angle dependency of the index and the variation of the index with cloud model. Ash model number 8, with extreme vertical distribution and fresh extinction, has the largest negativity. Models 3 and 8 are the only models easily distinguished from a cirrus cloud. The ash index difference is greatest at the smaller angles. Angles smaller than 120° did not work with the algorithm. Similar results were found for the land case, though a negative index was not produced for the ash cloud.

Two additional cases were run to see the variation in the index with land type. A desert case was run assuming a desert aerosol model and albedo with a tropical atmospheric model. A snow case was also run assuming a rural aerosol mode (visibility =23 km), mid-latitude winter atmospheric model, and fresh snow albedo. Figure 15 shows the desert case where the results are opposite of

what they are in all other cases, as the extreme ash conditions (8 and 3) are much more positive than the other cases. For the snow case (Figure 16) is similar to that of the desert with a smaller difference in indices for ash and meteorological clouds. Future work will be completed to establish the index values associated with differing ash and meteorological clouds. This study shows that although a negative index was not produced, the ash cloud index is significantly different from that of a meteorological cloud for the same conditions. These preliminary results show that the index of an ash cloud is much lower from that of a meteorological cloud over dark surfaces and higher over bright surfaces.

3.4.2 Dust/Sand Detection Module

More sensitivity studies need to be performed regarding the features of brightness temperatures shown in Figure 2 before making a definitive decision. Three kinds of tests have been designed to analyze sensitivity to the surface temperature, atmospheric profiles, surface albedo.

To investigate the sensitivity of the detection method to surface temperature, we allowed the surface temperature (T_s) to vary from 290K to 330K in steps of 5K and made a MODTRAN run for each step by keeping the other conditions the same as the case in Figure 2. When T_s is low (e.g., 290K), only $BT_{3.75}-BT_{8.55}$ will change from negative value to positive value when turbidity increases but $BT_{3.75}-BT_{10.8}$ and $BT_{3.75}-BT_{12.0}$ are always negative. When T_s is high (e.g., 330K), $BT_{3.75}-BT_{10.8}$ and $BT_{3.75}-BT_{12.0}$ will change from negative to positive value with the increase of turbidity and $BT_{3.75}-BT_{8.55}$ is always positive. For surface temperatures around 310K, $BT_{3.75}-BT_{8.55}$, $BT_{3.75}-BT_{10.8}$, and $BT_{3.75}-BT_{12.0}$ will change from negative to positive when turbidity increases as shown in Figure 2.

Sensitivity studies to atmospheric profiles are performed using four different atmospheric models of the MODTRAN radiation model, which include mid-latitude summer, tropical, mid-latitude winter, and sub-arctic winter atmospheres. Among these four atmospheres, mid-latitude summer is our baseline atmosphere. The tropical atmosphere is warmer and more moist than the other models. Both mid-latitude winter and sub-arctic winter atmospheres are colder and contain less moisture. Thus, these sensitivity tests may illustrate the response of brightness temperature of the four VIIRS thermal bands to different water vapor contents (the only significant gaseous absorber in the four channels) and temperature profiles. For two winter atmospheres, $BT_{3.75}-BT_{8.55}$, $BT_{3.75}-BT_{10.8}$, and $BT_{3.75}-BT_{12.0}$ will change from negative to positive when turbidity increases no matter whether the surface temperature is low (e.g., $T_s=290K$) or high (e.g., $T_s=330K$). For tropical atmosphere and lower surface temperature (e.g., $T_s=290K$), only $BT_{3.75}-BT_{8.55}$ changes from negative to positive at very large turbidity while $BT_{3.75}-BT_{10.8}$ and $BT_{3.75}-BT_{12.0}$ are always negative. When the surface temperature is between 300K and 330K, the features of difference in four brightness temperatures are similar to the baseline case as shown in Figure 9.

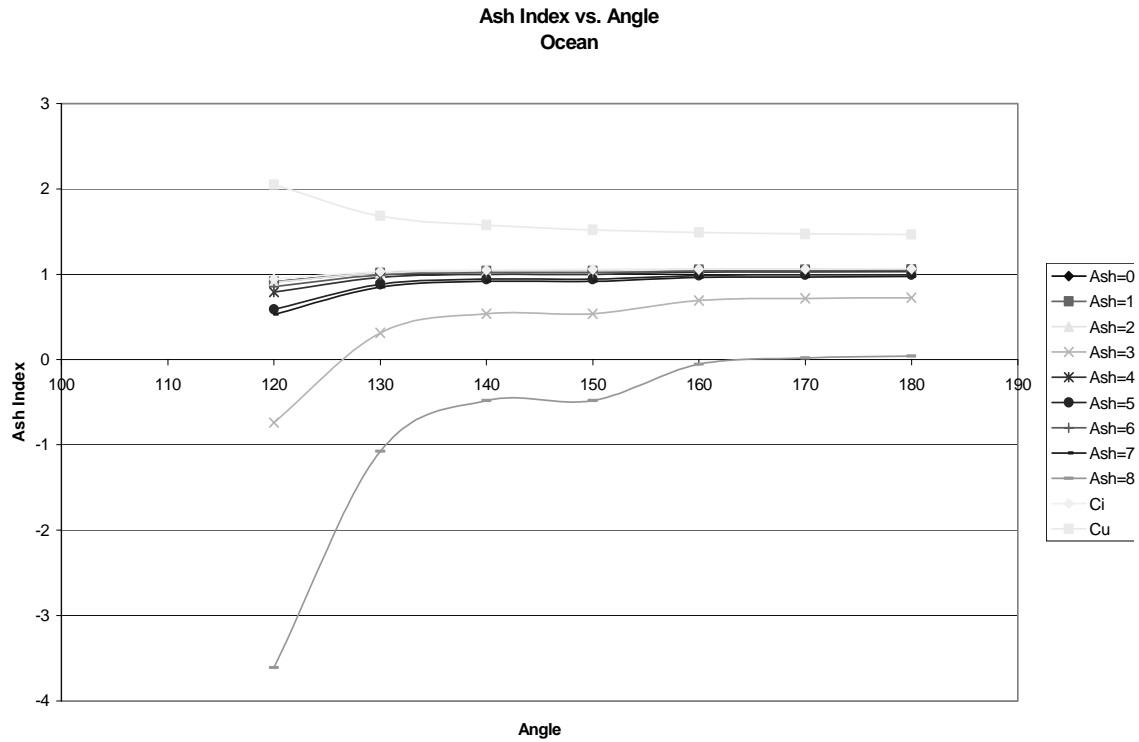


Figure 13. Derived ash indices ($BT_{10.8}-BT_{12.0}$) for the Ocean case.

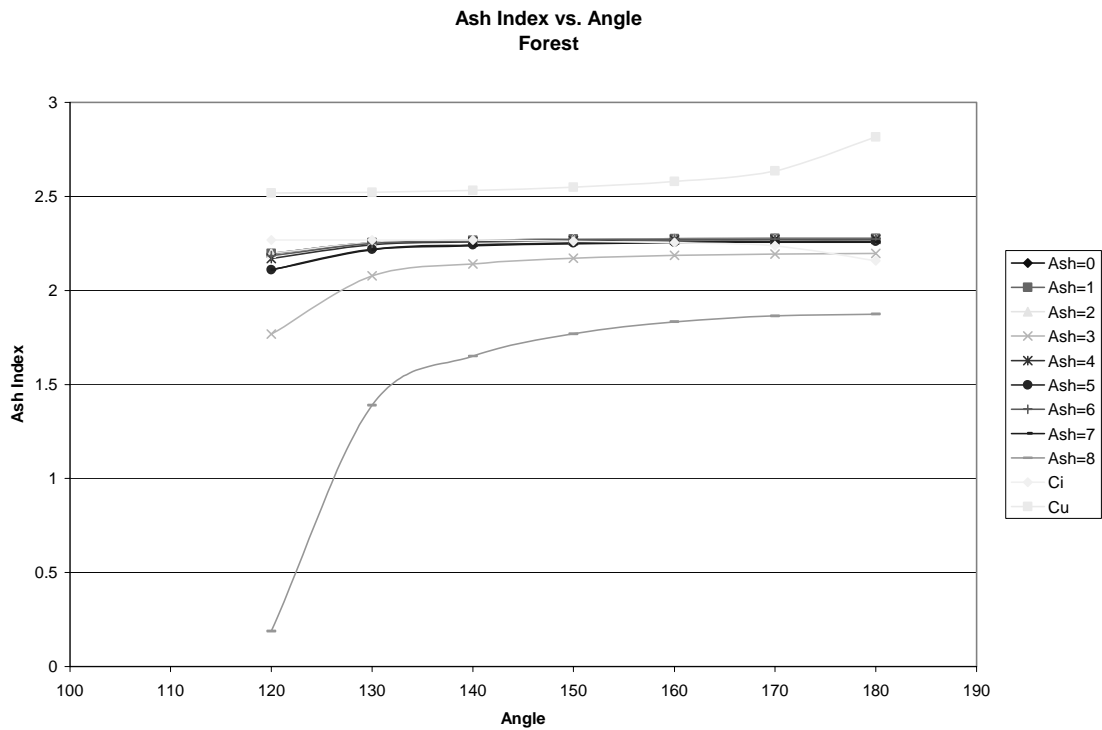


Figure 14. Derived ash indices for the Land case.

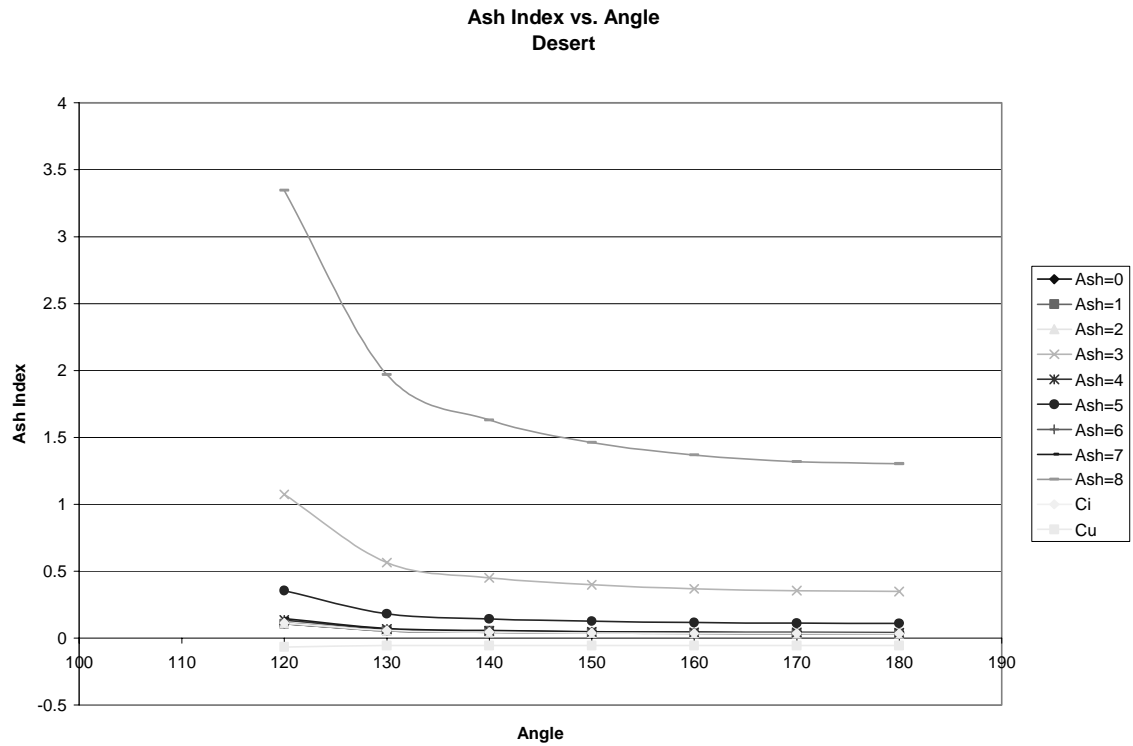


Figure 15. Derived ash indices for the Desert case.

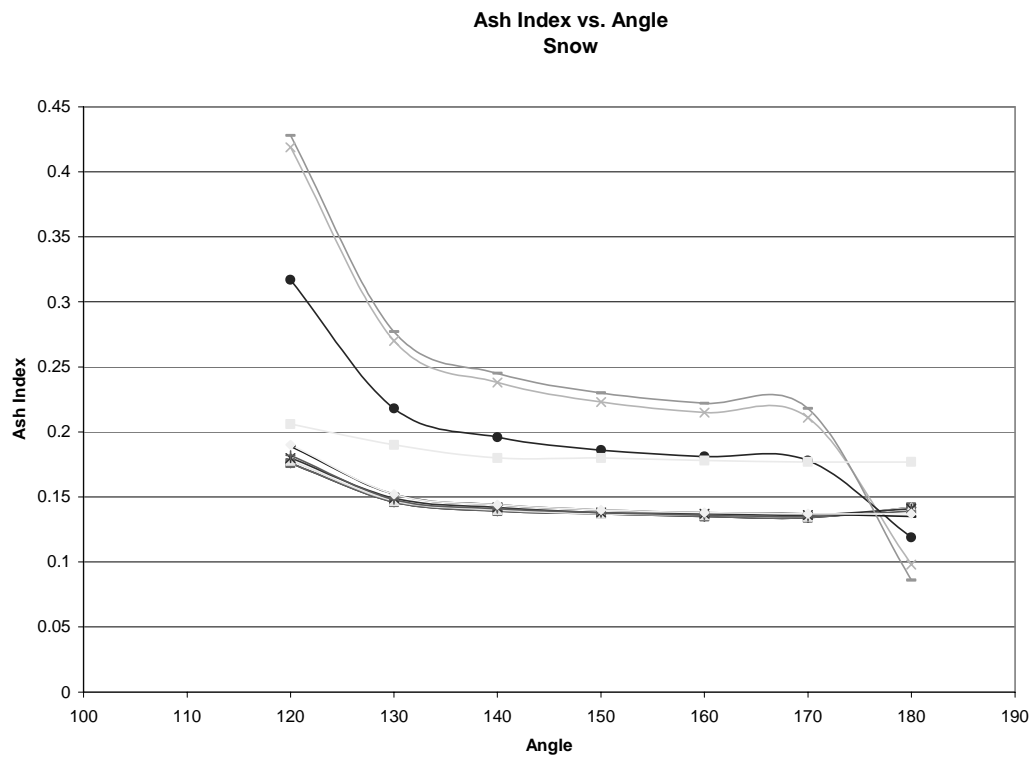


Figure 16. Derived ash indices for the Snow case.

Different surface albedos available in MODTRAN were also analyzed for dust detection sensitivity. Results indicate that as long as the surface is bright, either all three, two, or at least one of the brightness temperature differences among $BT_{3.75}-BT_{8.55}$, $BT_{3.75}-BT_{10.8}$, and $BT_{3.75}-BT_{12.0}$ will change from negative to positive when turbidity increases. However, for a dark surface (e.g., over ocean), $BT_{3.75}-BT_{8.55}$, $BT_{3.75}-BT_{10.8}$, and $BT_{3.75}-BT_{12.0}$ are always positive no matter how you change the turbidity or surface temperature. The reason for this is that the atmospheric transmission becomes dominant relative to the surface reflectance for a dark surface. Atmospheric transmission is larger at $3.75\ \mu\text{m}$ than in the other three channels because of the absorption characteristics of water vapor in these four thermal channels.

Based on the sensitivity studies and simulations above, we propose using a dust loading index (DLI) to detect a dust storm and identify its strength at night. When $BT_{3.75}-BT_{8.55}$, $BT_{3.75}-BT_{10.8}$, and $BT_{3.75}-BT_{12.0}$ are all positive, we set DLI equal to 3 to indicate the dust loading is heavy. When two out of the three brightness temperature differences are positive, we set DLI equal to 2 to represent medium dust loading. When only one of the three brightness temperature differences is positive, we set DLI equal to 1 to indicate that dust loading is very small. If none of the three brightness temperature differences are positive, we define DLI equal to zero to indicate that no dust appears. There may be some ambiguities in differentiating a scenario of $DLI = 0$ from that of $DLI = 1$. Because the dust loading in both scenarios is small, this does not present a problem. To further enhance our dust detection capability, we are going to combine the optical thickness derived from the visible channels at daytime with this approach at night. Moreover, meteorological conditions and geolocation information may also be utilized.

Further verification of our approaches for dust detection is necessary using real satellite-observed scenes of a dust storm. Thus, the remaining ambiguity can be further clarified. The results will be reported in future studies. We will also investigate the Wald *et al.* (1998) method more thoroughly.

3.4.3 Smoke Detection Module

The smoke detection algorithm is based on the spectral dependence of the aerosol reflectances from SeaWiFS measurement. SeaWiFS orbital data (counts) are used as the input along with some ancillary data sets, including the sensor calibration data, land and sea mask data, and surface elevation data. By combining this data with the corrections for Rayleigh scattering and ozone, oxygen, and water vapor absorption, and by choosing a proper projection scheme, we composed a global data set of the smoke index. The scheme has been successfully applied to detect the smoke from the Indonesian and Brazilian fires in 1997 (see Figure 17).

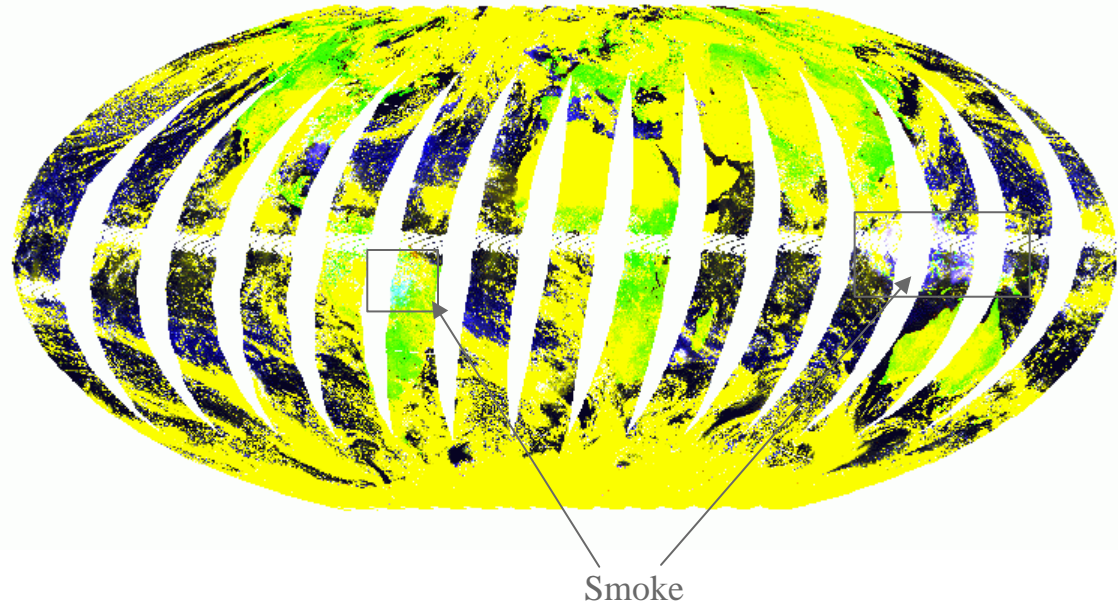


Figure 17. Global smoke index product using smoke detection module on SeaWiFS data for 22 September 1997. The smoke from fires over Indonesia was successfully detected (blue).

3.4.4 Comments on Major Errors

The algorithms used for detection of different types of suspended matter will involve both visible and IR-based techniques. Because radiances and brightness temperatures are involved, the sensitivity studies performed for the major errors listed in Section 3.3.12 will differ for each type of detection module. As there are no explicit detectability requirements for the types of suspended matter of interest, and as the capability to detect suspended matter will be a by-product of the capabilities required by other EDRs, we will not perform separate sensitivity studies for each type.

3.5 PRACTICAL CONSIDERATIONS

3.5.1 Numerical Computation Considerations

Requirements on processing speed and data storage are described in the VIIRS Computer Resources Requirements Document [Y3257].

3.5.2 Programming and Procedural Considerations

The procedural outline has been described in section 3.1.

3.5.3 Configuration of Retrievals

To avoid “hard-wiring” specific values into the operational software, a retrieval configuration file can be adopted in which the numerical values of adjustable parameters used within the retrievals (e.g., thresholds establishing whether a successful retrieval occurred) are stored.

3.5.4 Quality Assessment and Diagnostics

We have introduced a quality assurance (QA) flag which is stored at the resolution of the output EDR. The details of the QA Flag are as follows. Bits are numbered from 0 to 15 according to the Power of 2, bit 0 (2^0 , least significant), bit 15 (2^{15} : most significant)

Aerosol algorithm operational QA:

Bit 0:	Day/night flag : 0 day 1 (night)
Bit 1:	Internal Cloud mask result: 0 or 1 : 0 clear 1 Cloudy
Bit 2:	Land Water Mask: 0 (water) 1 (land)
Bit 3:	suspended matter identification: 0 passed 1 failed
Bit 4-5:	processing path for suspended matter: 00 (aerosol model) 01 (APSP) 10 (spectral test) 11 (spare)
Bit 6-7:	Sunglint: 00 (<0.1% ref) u01 (0.1%< ref <1.0%) 10 (ref >1.0%)

External Cloud Mask Results: At launch quality check

Bit 8:	External CM QA: 0 (determined) 1 (undetermined)
Bit 9-10:	External CM results: 4 bits: 00 confident clear, 01 prob clear, 10 prob cloudy 11 cloudy
Bit 11:	Multiple suspended matter type present: 0 (no) 1 (yes)

Spare bits:

Bit 12-15:	Spare
------------	-------

3.5.5 Exception Handling

Retrieval applicability is tested either on the pixel level or on a horizontal cell size level depending on the type. If a pixel or a cell is found to be unusable or contaminated according to a certain test, the remaining tests are not performed and the pixel or cell is discarded and flagged.

3.6 ALGORITHM VALIDATION

Modules of the retrieval algorithm will be verified pre-launch using data from existing satellite systems, such as Advanced Very High Resolution Radiometer (AVHRR), SeaWiFS, and Moderate Resolution Imaging Spectroradiometer (MODIS). We have successfully detected the smoke related to the large forest fires in Brazil and Indonesia during the summer of 1997 using the SeaWiFS data, and volcanic ash clouds using AVHRR data. More pre-launch validation will

be performed along with the update of detection modules. Post-launch verification will involve intercomparisons between VIIRS observations, ground-based measurements (e.g., Aerosol Robotic Network [AERONET]), and special airborne campaigns.

The required validation data for suspended matter will consist of data that describe as much as possible the aerosol layer much more than the optical thickness itself which is representative of the loading. The aerosol size distribution, which is inverted routinely for AERONET sites, will be a critical part of characterizing the aerosol type. The information provided by AERONET, provided its reliability has been established, can be directly translated in most cases in one of the suspended matter category because they provide in addition to the size distribution, the absorption (single scattering albedo) and real refractive index at several wavelengths (0.45 μ m to 1.02 μ m). Other measurements typically taken during validation campaign, will help augment or validate the AERONET measurements, typically independent estimation of aerosol size distribution (through particle counters), electronic microscopy analysis of particle size and shape deposited on filters, chemical characterization, independent measurements of absorption properties, aerosol profiles by Light Detection and Ranging (LIDARs).

4.0 ASSUMPTIONS AND LIMITATIONS

4.1 ASSUMPTIONS

Assumptions in the retrieval of aerosol optical thickness and size parameter are applicable to the retrieval of suspended matter (VIIRS Aerosol Optical Thickness and Size Parameter Algorithm Theoretical Basis Document [V-2]). As the types of suspended matter are not completely defined within the SRD, we have stated our own definitions of the suspended matter types within this document.

4.2 LIMITATIONS

The suspended matter SRD requirements call for a threshold of typing within the atmosphere total column, and an objective of typing the suspended matter within specified 0.2 km layers of the atmosphere. Determining the amount of suspended matter within layers will be difficult to achieve, and impossible with VIIRS data alone. We may utilize the OMPS UV radiances for absorbing aerosols to determine their vertical distribution. We could use the OMPS limb-scanning information to determine vertical distribution, but this data would only be useful down to the cloud tops. One potential problem in using the OMPS data is the 50 km horizontal resolution of the OMPS aerosol index and ozone products. The suspended matter horizontal cell size is required to be 3 km or smaller. All the retrievals will be performed under clear conditions.

5.0 REFERENCES

- Ackerman S.A. (1997). Remote sensing of aerosols using satellite infrared observations. *Journal of Geophysical Research-Atmospheres*, 102: (D14) 17069-17079.
- Ackerman S.A. (1989). Using the radiative temperature difference at 3.7 and 11 μ m to track dust outbreaks. *Remote Sensing of Environment*, 27: (2) 129-133.
- Ackerman S.A., and K.I. Strabala (1994). Satellite remote-sensing of H₂SO₄ aerosol using the 8 μ m to 12 μ m window region - application to Mount Pinatubo. *Journal of Geophysical Research-Atmospheres*, 99: (d9) 18639-18649.
- Ardanuy, P. E., and H. L. Kyle (1986). Observed Perturbations of the Earth's Radiation Budget: A Response to the El Chichón stratospheric Aerosol Layer, *J. Climate Appl. Meteor.*, 25, 505-516.
- Barton I.J., A.J. Prata, I.G. Watterson, and S.A. Young (1992). Identification of the Mount Hudson volcanic cloud over SE Australia. *Geophysical Research Letters*, 19: (12) 1211-1214.
- Bolin, B., J. Houghton, and L. G. M. Filho; ed. (1994). Radiative Forcing of Climate Change, Intergovernmental Panel on Climate Change (IPCC), UNEP, World Meteorol. Organ., Geneva.
- Bredow, J., R. Proco, M. Dawson, C. Betty, S. Self, and T. Thordarson (1995). A multifrequency laboratory investigation of attenuation and scattering from volcanic ash clouds. *IEEE Trans. Geosci. Remote Sens.*, 33, 1071-1081.
- Charlson, R. J., S. E. Schwartz, J. M. Hales, R. D. Cess, J. A. Coackley Jr., J.E. Hansen, and D. J. Hofman (1992). Climate forcing of anthropogenic aerosols. *Sciences*, 255, 423-430m.
- d'Almeida, G.A., P. Koepke, and E.P. Shettle (1991). Atmospheric aerosols: Global climatology and radiative characteristics. A. Deepak Publishing, Hampton, Virginia.
- Harris, D., and W. Rose (1983). Estimating particle sizes, concentrations, and total mass of ash in volcanic clouds using weather radar. *J. Geophys. Res.*, 88, pp. 10,969-10,983.
- Iqbal, M. (1983). An Introduction to Solar Radiation. Academic Press, New York
- Kaufman, Y.J., A. Setzer, D. Ward, D. Tanre, B.N. Holben, P. Menzel, M.C. Pereira, and R. Rasmussen (1992). Biomass burning Airborne and Spaceborne experiment in the Amazonas (BASA-A). *J. Geophys. Res.*, 97, pp. 14, 581-14,599.
- Kaufman, Y. J., D. Tanre, L. A. Remer, E. F. Vermote, A. Chu, and B. N. Holben (1997). Operational remote sensing of tropospheric aerosol over land from EOS moderate resolution imaging spectroradiometer. *J. Geophys. Res.*, 102, 1,6971-1,6988.

- Legrand M., J.J. Bertrand, M. Desbois, L. Menenger, and Y. Fouquart (1989). The potential of infrared satellite data for the retrieval of Saharan-dust optical depth over Africa, *Journal of Applied Meteorology*, 28: (4) 309-319.
- Longtin, D.R., E.P. Shettle, J.R. Hummel, and J.D. Pryce (1988). A wind dependent desert aerosol model: Radiative Properties, AFGL-TR-88-0112.
- Morales, C., ed. (1979). Saharan Dust: mobilization, transport, deposition: papers and recommendations from a workshop held in Gothenburg, Sweden, 25-28 April 1977, pp. 297.
- Péwé, T. L. (1981). Desert Dust: Origin, Characteristics, and Effect on Man, Geological Society of America, Special Paper 186.
- Prata, A.J. (1989). Infrared radioactive transfer calculations for volcanic ash clouds. *Geophy. Research Letters*, 16, 1293.
- Private Forest Management Team, Auburn University, Alabama, (1999). (<http://www.pfmt.org/standman/smokeman.htm>)
- Rose, W., A. Kostinski, and L. Kelley (1995a). Real time C-band radar observations of 1992 eruption clouds from Crater Peak/Spurr volcano, Alaska. U.S. Geol. Surv. Bull., 2139, pp. 19-26.
- Shenk W.E., and R.J. Curran (1974). Detection of dust storms over land and water with satellite visible and infrared measurements, *Monthly Weather Review*, 102: (12) 830-837.
- Simarski, L. (May 1992). Volcanism and climate change. *Amer. Geophys. Union*.
- Stowe, L., R. Carey, and P. Pellegrine (Jan 24, 1992). Monitoring the Mt. Pinatubo aerosol layer with NOAA/11 AVHRR data. *Geophys. Res. Lett.*, 19, no. 2, 159-162.
- Tegen I. and I. Fung (1995). Contribution to the atmospheric mineral aerosol load from land-surface modification, *Journal of Geophysical Research Atmospheres*, 100:(D9) 18707-18726.
- Tanré, D., and M. Legrand (1991). On the satellite retrieval of Saharan dust optical thickness over land: two different approaches, *J. Geophys. Res.*, 96, 5221-5227.
- Tanre D., P.Y. Deschamps, C. Devaux, and M. Herman (1988). Estimation of Saharan aerosol optical thickness from blurring effects in Thematic Mapper data, *Journal of Geophysical Research-Atmospheres*, 93: (D12) 15955-15964.
- Vermote, E., C. O. Justice, J. Descloitres, N. El Saleous, J. Ray, D. Roy, B. Margerin, and L. Gonzalez (2001). A Global Monthly Coarse Resolution Reflectance Data Set from SeaWiFS for use in Land, Ocean, and Atmosphere applications, *International Journal of Remote Sensing*, 22: (6) 1151-1158.

- Vermote, E., D. Tanre, J. L. Deuze, M. Herman, and J. J. Morcrette (1997). Second Simulation of the Satellite Signal in the Solar Spectrum (6S). 6S User Guide Version 2, 217 pp.
- Wald, A.E., Y.T. Kaufman, D. Tanré, and B.C. Gao (1998). Daytime and nighttime detection of mineral dust over desert using infrared spectral contrast. *J. Geophys. Res.*, 103, 32307-32313.
- Wen S. and W.I. Rose, Retrieval of particle sizes and total masses in volcanic clouds using AVHRR bands 4 and 5, Poster presented at AGU 1993 Fall Meeting.